



**HAL**  
open science

# Numerical investigation of spreading time in droplet impact with spherical surfaces: from physical analysis to data-driven prediction model

Ikroh Yoon, Seungwon Shin, Damir Juric, Jalel Chergui

## ► To cite this version:

Ikroh Yoon, Seungwon Shin, Damir Juric, Jalel Chergui. Numerical investigation of spreading time in droplet impact with spherical surfaces: from physical analysis to data-driven prediction model. *Theoretical and Computational Fluid Dynamics*, 2024, 38 (2), pp.225-250. 10.1007/s00162-024-00698-x. hal-04647253

**HAL Id: hal-04647253**

**<https://hal.science/hal-04647253v1>**

Submitted on 13 Jul 2024

**HAL** is a multi-disciplinary open access archive for the deposit and dissemination of scientific research documents, whether they are published or not. The documents may come from teaching and research institutions in France or abroad, or from public or private research centers.

L'archive ouverte pluridisciplinaire **HAL**, est destinée au dépôt et à la diffusion de documents scientifiques de niveau recherche, publiés ou non, émanant des établissements d'enseignement et de recherche français ou étrangers, des laboratoires publics ou privés.

1 **Numerical investigation of spreading time in droplet impact with**  
2 **spherical surfaces: from physical analysis to data-driven**  
3 **prediction model**

4  
5  
6 Ikroh Yoon<sup>1,a</sup>, Seungwon Shin<sup>2</sup>, Damir Juric<sup>3,4</sup> and Jalel Chergui<sup>3</sup>

7  
8 <sup>1</sup> Korea Institute of Marine Science and Technology Promotion (KIMST), 06775 Seoul,  
9 Korea (currently works at Intergovernmental Oceanographic Commission of United Nations  
10 Educational, Scientific and Cultural Organization, 75007 Paris, France), [iryoon@kimst.re.kr](mailto:iryoon@kimst.re.kr)

11  
12 <sup>2</sup> Department of Mechanical and System Design Engineering, Hongik University, 04066  
13 Seoul, Korea, [sshin@hongik.ac.kr](mailto:sshin@hongik.ac.kr)

14  
15 <sup>3</sup> Centre National de la Recherche Scientifique (CNRS), Laboratoire Interdisciplinaire des  
16 Sciences du Numérique (LISN), Université Paris Saclay, 91400 Orsay, France,  
17 [Damir.Juric@lisn.fr](mailto:Damir.Juric@lisn.fr), [Jalel.Chergui@lisn.fr](mailto:Jalel.Chergui@lisn.fr)

18  
19 <sup>4</sup> Department of Applied Mathematics and Theoretical Physics, University of Cambridge,  
20 Centre for Mathematical Sciences, Wilberforce Road, Cambridge CB3 0WA, UK

21  
22 <sup>a)</sup> Corresponding Author:

23 Senior researcher, Ikroh Yoon, PhD

24 E-Mail: [iryoon@kimst.re.kr](mailto:iryoon@kimst.re.kr)

## ABSTRACT

Spreading time, the time that an impacting droplet attains the maximum wetting area on a solid surface, plays a critical role in many engineering applications particularly where heat transfer or chemical reactions are involved. Although the impact dynamics of a droplet significantly differ across the different spreading regimes depending on various collision parameters, it still remains unclear (i) how the spreading time changes for each spreading regime, and (ii) how the target curvature can affect the spreading time. In the present study, the spreading time during droplet impact on a spherical target is systematically studied at the three different spreading regimes for a wide range of impact parameters (Weber number, equilibrium contact angle, Ohnesorge number and droplet-to-target size ratio). The changes of spreading time depending on the impact parameters and underlying physical mechanisms are analyzed in detail at the level of three different spreading regimes. Our results show that the spreading time, proper time scales, dominant impact parameters and associated physical behaviors all significantly and non-linearly change across the three spreading regimes. An improved prediction model for the spreading time is also proposed for each regime, which is now based on only the controllable variables and has an explicit form. The effect of target curvature on the spreading time is further investigated, and finally, a data-driven prediction model is proposed to represent the complicated and non-linear nature of the spreading time broadly across the three spreading regimes.

Keywords: droplet impact; spreading time; multiphase flow simulation; prediction model; data-driven analysis

## 47 I. INTRODUCTION

48

49 Collisions of droplets with **solid surfaces** can be found not only in a broad range of  
50 modern technologies but also in everyday life [1,2]. Since droplet collision phenomena can  
51 play crucial roles in the performance of diverse engineering applications such as spray  
52 cooling and chilling [3], spray drying [4], wet-scrubbers [5], fluid catalytic cracking (FCC)  
53 [6], trickle-bed reactors [7], microfluidic-based encapsulation of biomaterials [8] and tablet  
54 coating [9], to name a few examples, their collision processes have naturally been of great  
55 interest across various fields of chemical, mechanical, pharmaceutical, food and bio  
56 industries [1,9-11]. In general, the collision behavior is dominated by a complicated  
57 competition and interaction among inertial, viscous, and capillary forces (sometimes  
58 including the gravitational force as well) at very small length and time scales [12,13].

59 For droplet impact problems with a solid surface much effort has focused on  
60 investigating the maximum spreading extent (normally characterized by the maximum  
61 spreading diameter) [14-17] and the spreading time [18-21]. The former measures “how  
62 much a droplet can spread over a target surface”, while the latter quantifies “how long it takes  
63 to reach the maximum spreading state”. Both quantities usually play critical roles in  
64 determining process performance and efficiency particularly in the context of controlling the  
65 droplet deposition process [1,12,19]. For example, the maximum spreading extent of a  
66 catalyst particle significantly affects the catalyst efficiency as well as the system performance  
67 of trickle-bed reactors [7] and the spreading time also plays an important role in collision  
68 processes where heat transfer (e.g., droplet solidification) [14] and/or chemical reactions  
69 (e.g., cracking reaction in the FCC system) [22] are involved.

70 After Chandra and Avedisian’s work [23] which has initiated a series of energy-balance-

71 based theoretical approaches for estimating the maximum spreading diameter of droplets  
72 numerous studies have been devoted to the spreading dynamics of droplets on a solid surface.  
73 Based on the concept of the energy-balance between the collision instant and the maximum  
74 spreading state Pasandideh-Fard *et al.* [24] proposed more refined length and time scales to  
75 evaluate the energy loss in the boundary layer where the viscous dissipation occurs and their  
76 approach has indeed provided a cornerstone for many later theoretical energy-balance-based  
77 approaches [25,26]. This type of analysis was also widely utilized for estimating the rebound  
78 criteria of bouncing droplets on a non-wettable surface [25] as well as the maximum  
79 spreading extent [23-26]. Afterward, Roisman [27] considered the full Navier-Stokes  
80 equations to estimate the flow field inside the droplet and proposed a semi-empirical model  
81 using the experimentally fitted data. Later, his model was experimentally demonstrated to be  
82 one of the most accurate models for the maximum spreading extent for a wide range of  
83 Weber number and surface wettability [14]. Wilderman *et al.* [17] presented an interesting  
84 analysis for high-speed drop impact problems. They showed that roughly one-half of the  
85 initial (impact) kinetic energy can be converted into surface energy owing to a universal head  
86 loss regardless of detailed impact conditions and energy dissipation mechanisms. More  
87 recently some other sources causing extra energy loss during the spreading stage of droplets  
88 have been found to affect the maximal spreading extent, e.g., residual kinetic energy in the  
89 form of vortical flow inside a droplet [16] or energy loss due to ‘interface relaxation’ near a  
90 solid surface [18]. Although there is still a debate on the maximum spreading extent [28], in  
91 general, scaling laws of  $We^{1/4}$  derived from momentum conservation [16] and  $We^{1/2}$  derived  
92 from energy conservation [29] have been experimentally shown to hold for the inviscid  
93 regime (for less viscous droplets) whereas a  $Re^{1/5}$  rule [30] has worked well for a viscous  
94 regime (for highly viscous droplets).

95 There have also been several attempts to examine spreading dynamics for droplet

96 collision on curved surfaces such as a spherical target. Bakshi *et al.* [31] experimentally  
97 showed that the film thickness at the collision center undergoes three different phases: (i)  
98 initial drop-deformation, (ii) inertia-dominated and (iii) viscosity-dominated. The  
99 dimensionless film thickness profiles were collapsed on a single curve for the first and second  
100 phases. Malgarinos *et al.* [32] used volume-of-fluid (VOF) simulation to study the problem of  
101 drop collision on spherical targets. They investigated the boundary separating the coating  
102 from the rebound regime, the film thickness, and the wetted area. Afterward, they further  
103 performed extensive VOF simulations to study drop impact on a spherical particle including  
104 phase change and reaction phenomena in a high temperature environment ( $T \geq 800$  K) [33].  
105 Zhang *et al.* presented two-dimensional [34] and three-dimensional [35] Lattice-Boltzmann  
106 simulations. They examined the effects of Weber and Reynolds numbers on the film thickness  
107 at the collision center, and their simulation results reproduced Bakshi *et al.*'s [31]  
108 experimental observations well. Liang *et al.* [36] experimentally studied drops impacting on  
109 wetted spherical targets, and they showed the drop-to-target curvature ratio played a critical  
110 role in not only the spreading characteristics but also determining the splashing threshold.  
111 Mitra *et al.* [37], Liu *et al.*, [38], and Khurana *et al.* [39] proposed energy-balance-based  
112 prediction models for evaluating the spreading extent on a spherical surface and their models  
113 reproduced their experimental observations well. Yoon and Shin [40] also proposed scaling  
114 laws and an empirical correlation for the maximum spreading diameter of a droplet colliding  
115 with a spherical surface for a wide range of liquid viscosity. More recently, Yoon *et al.* [41]  
116 proposed a data-driven prediction model for the maximum spreading that can be applied to  
117 both a flat surface and a spherical surface. Although these studies reviewed above have  
118 provided useful relations to estimate the maximum spreading extent as well as have notably  
119 shed light on our understanding of the physical mechanisms of spreading droplets, they have  
120 mainly focused on the maximum spreading extent itself rather than on the spreading time.

121 We now review studies in the context of the spreading time which has been relatively  
122 less well-explored compared to the maximum spreading extent. Although it has long been  
123 understood that the contact time of a droplet is limited by the Rayleigh oscillation time [42]  
124 which is a function of the drop's density, diameter and surface tension coefficient, the energy-  
125 balance-based approaches, at the very early stage, simply approximated the spreading time  $\tau$   
126 ignoring the effect of surface tension. Chandra and Avedisian [23] considered  $\tau$  to be  $\tau = D_d /$   
127  $V_{ini}$ , where  $D_d$  and  $V_{ini}$  are the initial droplet diameter and the impact velocity, respectively.  
128 This is indeed the advective characteristic time scale which has normally been used to  
129 nondimensionalize the physical time scale [31], and also can be interpreted as the required  
130 time for a droplet to reach zero height from its initial diameter,  $D_d$ , at a constant impact  
131 velocity  $V_{ini}$ . Pasandideh-Fard *et al.* [24] modified the spreading time to be  $\tau = 8D_d / 3V_{ini}$   
132 based on a simple geometric assumption and mass conservation and their model has been  
133 widely used in many other theoretical studies [26,43]. Recently, Antonini and Amirfazli [14]  
134 experimentally showed that the spreading time  $\tau$  is considerably affected by surface  
135 wettability. Lee *et al.* [44] also presented significant effects of liquid properties on  $\tau$ . They  
136 replaced the initial drop diameter ( $D_d$ ) in Pasandideh-Fard *et al.*'s model [24] with  $D_m$  (where  
137  $D_m$  is the maximum spreading diameter), suggesting an empirical model,  $\tau = b(D_m/V_{ini})$ ,  
138 where  $b$  is the ratio of the surface tension coefficient between a working droplet and a water  
139 droplet. Huang and Chen [18] and Wang *et al.* [45] also adopted a similar spreading time as  
140 the model of Lee *et al.* [44]. Lin *et al.* [19] presented a remarkable experimental study for the  
141 spreading time and systematically analyzed the effects of various collision parameters (e.g.,  
142 impact velocity, liquid properties and surface wettability) on  $\tau$  for a very wide range of  
143 collision conditions. They also proposed a new empirical model for the spreading time as a  
144 function of Weber number, i.e.,  $\tau^* = 0.92We^{-0.43}$ . Here,  $\tau^*$  is the rescaled spreading time using  
145 a modified capillary time scale  $(\rho D_m^3/8\sigma)^{0.5}$  based on the maximal spreading diameter,  $D_m$ ,

146 where  $\rho$  and  $\sigma$  are the density of a droplet and the surface tension coefficient, respectively. Du  
147 *et al.* [21] also proposed a similar empirical model ( $\tau^* = 1.47We^{-0.44}$ ) as Lin *et al.*'s model  
148 [19]. More recently, Aksoy *et al.* [20] showed the effect of liquid viscosity on the spreading  
149 time and proposed an empirical model as a function of both Weber and Reynolds number, i.e.,  
150  $\tau^* = 2We^{-0.45}Re^{-0.09}$ .

151 Even considering the numerous studies heretofore undertaken, it still remains difficult to  
152 comprehensively understand how the spreading time of a droplet can be affected by various  
153 collision parameters for a wide range of impact parameters. In particular, one can find  
154 significant knowledge gaps as follows:

155

156 (i) It is well-known that drop spreading dynamics vary significantly across the  
157 different spreading regimes. For example, a drop's physical behavior and its  
158 maximum spreading extent change considerably across inviscid and viscous  
159 regimes [16,29,30]. However, it is still unclear how the spreading time ( $\tau$ )  
160 changes for different spreading regimes, because the existing studies have usually  
161 studied the global behavior of spreading time at a general level, not focused on  
162 detailed changes and associated physical mechanisms at the level of each  
163 different spreading regime.

164

165 (ii) Although the significant effects from impact parameters (e.g., We, Re, surface  
166 wettability, etc.) on the spreading time have been evidently demonstrated by  
167 many experiments [14,18-20,44], it is not easy yet to model the spreading time  
168 using those impact parameters. All recent scaling laws (or empirical models)  
169 reviewed above [18-21,44,45] have still been a function of the maximum  
170 spreading diameter ( $D_m$ ) which is usually unknown. Since the effects of impact



171 parameters are already reflected in  $D_m$  [14-17,25,27],  $D_m$  cannot be considered as  
172 a controllable independent variable to model  $\tau$  resulting in the limitation of direct  
173 “physical interpretation” of relations between the impact parameters and the  
174 spreading time. In addition, the existing models [18-21,44,45] cannot be  
175 explicitly solved due to the multiple unknown variables (i.e., the maximum  
176 spreading diameter and the spreading time) leading to inconvenience for users.

177  
178 (iii) The effect of surface curvature on the spreading time has not been systematically  
179 investigated so far. Although a few recent numerical studies [46,47] have  
180 demonstrated that the surface curvature can affect the spreading time of the  
181 droplet collision system, it is still unclear that how the spreading time changes  
182 depending on the surface curvature for different spreading regimes. In addition,  
183 to the best of our knowledge, there has not yet been a prediction model for the  
184 spreading time which can consider the effect of surface curvature.

185  
186 In this study, we expand our previous work [41] which examined the maximum  
187 spreading extent, now focusing on the systematic investigation of the spreading time which is  
188 another important design parameter in the droplet collision system. Based on our verified  
189 computational framework, effects of important impact parameters (i.e., collision velocity,  
190 surface wettability, liquid viscosity, surface tension and surface curvature) on the spreading  
191 time are quantified for a wide range of impact parameters. In particular, detailed changes in  
192 the spreading time and associated underlying mechanisms are analyzed for three different  
193 spreading regimes to better understand the complicated physical behaviors. A new prediction  
194 model for the spreading time using only controllable independent variables is presented for  
195 each regime, and a data-driven prediction model for the entire spreading regime is also

196 proposed broadly covering all ranges of impact parameters considered in the present study.

197 The remainder of the current paper is organized as follows: Section II provides a brief  
198 introduction of the simulation methods used herein. Section III quantitatively and  
199 systematically examines the spreading time of a droplet collision system. Physical analysis  
200 and prediction models are also presented in this section. The major findings are summarized  
201 in Section IV.

202

## 203 II. COMPUTATIONAL FORMULATION

204

205 Since we primarily focus on understanding the physical characteristics of the spreading  
206 time, and have utilized the same computational framework as in our previous studies  
207 [40,41,48,49], we provide here a brief introduction of our numerical methods used in this  
208 study rather than a fully detailed explanation. For more algorithmic details and relevant  
209 techniques on our simulation methods, and for our various benchmark tests including grid  
210 convergence characteristics, readers can refer to our previous work [40,41,48,49]. Note also  
211 that our computational framework has been extensively applied to diverse droplet collision  
212 cases for various types of solid surface including flat substrates [49], spherical objects  
213 [40,41,48], cylindrical targets [50] and has also been streamlined (using an adaptive-mesh-  
214 refinement approach [51]) and parallelized [52].

215 For incompressible flows the governing equations can be applied to all three phases  
216 (solid, liquid and gas) and are solved on a fixed Cartesian (Eulerian) grid as a single-field  
217 formulation:

218

$$219 \quad \nabla \cdot \mathbf{u} = 0 \quad (1)$$

220

$$\rho \left[ \frac{\partial \mathbf{u}}{\partial t} + \mathbf{u} \cdot \nabla \mathbf{u} \right] = -\nabla P + \rho \mathbf{g} + \nabla \cdot \mu (\nabla \mathbf{u} + \nabla \mathbf{u}^T) + \mathbf{F} \quad (2)$$

222

223 where  $\mathbf{u}$ ,  $P$  and  $\mathbf{g}$  are the velocity vector, the pressure, and the gravitational acceleration,  
224 respectively.  $\rho$  is the density and  $\mu$  is the viscosity. The surface tension force  $\mathbf{F}$  is considered  
225 only at the phase (gas-liquid) interface and can be modeled by the following hybrid  
226 representation based on the continuum-surface-force (CSF) formulation [53]:

227

$$\mathbf{F} = \sigma \kappa_H \nabla I \quad (3)$$

229

230 where  $\kappa_H$  is the curvature field. Note that  $I$  is the indicator function which has the  
231 characteristics of the Heaviside function, varying from 0 (zero) in one phase (liquid droplet)  
232 to 1 (one) in the other phase (ambient air).

233 The physical properties of both phases (i.e., the ambient air and the liquid droplet) can  
234 also be assigned by using the indicator function  $I$  as follows:

235

$$\rho = \rho_d + (\rho_a - \rho_d) I \quad (4)$$

237

$$\mu = \mu_d + (\mu_a - \mu_d) I \quad (5)$$

239

240 Here, the subscript “d” denotes droplet, whereas “a” denotes air. Note that this common  
241 approach has been broadly applied to various multiphase-flow simulations and more detailed  
242 techniques dealing with the surface tension force and the physical properties near the gas-  
243 liquid phase interface can be found in Unverdi and Tryggvason [54] and Brackbill *et al.* [53].

244 Our dynamic contact angle modeling technique is given in Appendix A, and further details of  
245 the discretization of the governing equations, time-stepping, and other solution techniques  
246 used in the present study can also be found in Yoon *et al.* [41] and Yoon and Shin [48].

247 One of the most essential algorithms for this type of multiphase-flow simulation is an  
248 interface tracking method. Here we use the level contour reconstruction method (LCRM) [55-  
249 57] to track the gas-liquid phase interface. The LCRM is a hybrid method benefitting from  
250 two of the most well-established and popular interface tracking methods, i.e., level set [58]  
251 and front tracking [54]. In the LCRM the phase interface is basically represented by using  
252 (Lagrangian) moving marker elements (lines in 2D simulations and triangles in 3D  
253 simulations, as in the original front tracking method) but the moving elements are re-meshed  
254 using the distance function which is the key feature of the level set method. Such a  
255 reconstruction procedure can allow us to avoid the algorithmic complexity of dealing with the  
256 connectivity among the moving interface elements which is the most well-known  
257 shortcoming of the original front tracking method. Note that each moving element can always  
258 be implicitly (naturally) interconnected without any further artificial connection technique  
259 because the reconstruction procedure is performed at each boundary between cells (i.e., at  
260 cell faces) on the fixed Cartesian grid. Note also that the LCRM retains the tracking  
261 capability of the original front tracking method (i.e., accurate representation of the phase  
262 interface using moving markers) while avoiding the complex algorithmic difficulties in  
263 handling the topology changes (e.g., deformation, pinch-off or coalescence of the phase  
264 interface). For more details on the LCRM readers can refer to Shin and Juric [55,56].

265 Figure 1 illustrates the simulation geometry and boundary conditions used in this study.  
266 All simulations are performed in a (two-dimensional) axi-symmetric domain. The axi-  
267 symmetric boundary condition is set for the left boundary whereas open boundary conditions  
268 are set for the right, upper and lower boundaries. The lengths of the physical domain are set

269 as  $R_L = 7.5$  (in the radial  $r$  direction) and  $Z_L = 20$  (in the axial  $z$  direction) times the droplet  
 270 radius, respectively, which are sufficiently large compared to the size of the droplet. **Note that**  
 271 **near the splashing threshold [59,60] the droplet rim may exhibit considerable asymmetric**  
 272 **behavior along the circumferential direction (e.g., fingering or cusp of lamella [12,13]).**  
 273 **Therefore, we set the simulation conditions sufficiently below the splashing threshold**  
 274 **(specific conditions will be described later) to ensure that our axi-symmetric formulation can**  
 275 **be a reasonable approach to reducing the necessary computational resources [41,51]. A**  
 276 droplet impacts onto a stationary spherical **target** at an initial impact velocity, ( $V_{ini}$ ) and  $D_s$  is  
 277 the diameter of the **spherical target** where the subscript “s” denotes the **target surface**.  
 278

### 279 **III. RESULTS AND DISCUSSION**

280  
 281 The spreading dynamics of a droplet on a solid surface is primarily dominated by a  
 282 complicated time-and-space dependent interplay among inertial, viscous, and capillary effects  
 283 [12,13] and to characterize their relative importance, three non-dimensional variables, i.e., the  
 284 Weber number ( $We = \rho_d V_{ini}^2 D_d / \sigma$ ), the Reynolds number ( $Re = \rho_d V_{ini} D_d / \mu_d$ ) and the  
 285 Ohnesorge number [ $Oh = \mu_d / (\rho_d \sigma D_d)^{0.5}$ ] have usually been used. Because Oh can also be  
 286 represented by using We and Re (i.e.,  $Oh = We^{0.5} / Re$ ) the spreading dynamics can basically  
 287 be characterized by two of these numbers. Here we use We and Oh as impact parameters with  
 288 two other variables, i.e., the equilibrium contact angle ( $\theta_{eqi}$ ) and the droplet-to-**target** size  
 289 ratio ( $\Omega$ ) which characterize surface wettability and the curvature of the **target surface**,  
 290 respectively.

291 Three characteristic time scales are considered, i.e., the advective time,  $t_a = D_d / V_{ini}$   
 292 [30,61], the capillary time,  $t_c = (\rho_d D_d^3 / 8\sigma)^{0.5}$  [16,62], and the viscous time.  $t_v = \mu_d D_d / \sigma$  [16,62].  
 293 The physical time scale,  $t$ , can be non-dimensionalized by the three characteristic time scales

294 above and the non-dimensional advective, capillary, and viscous time scales are denoted by  
295  $t_a^*$  ( $t_a^* = t / t_a$ ),  $t_c^*$  ( $t_c^* = t / t_c$ ),  $t_v^*$  ( $t_v^* = t / t_v$ ), respectively.

296 To sufficiently cover the broad range of impact parameters, and to systematically  
297 examine the effects of impact parameters on the spreading time, we consider a total of 2400  
298 collision cases. The droplet diameter and the density are fixed at  $D_d = 2$  mm and  $\rho_d = 998.2$   
299 kg/m<sup>3</sup>, respectively. The physical properties of the gas phase (ambient air) and the surface  
300 tension coefficient are also fixed ( $\rho_a = 1.2$  kg/m<sup>3</sup>,  $\mu_a = 0.000018$  N s/m<sup>2</sup>, and  $\sigma = 0.0728$  N/m).

301 Four collision parameters, i.e.,  $We$ ,  $Oh$ ,  $\theta_{eqi}$  and  $\Omega$  are varied by controlling the impact  
302 velocity ( $V_{ini}$ ), droplet viscosity ( $\mu_d$ ), equilibrium contact angle ( $\theta_{eqi}$ ) and the diameter of the  
303 target ( $D_s$ ), respectively. The splashing threshold is usually described by  $We$  and  $Oh$  [59,63],  
304 and splashing can be observed more easily on a small spherical target compared to that on a  
305 flat substrate [63]. Since splashing can occur near  $We \sim 150 - 160$  if  $\Omega \sim 1/4 - 1/2$  (for  
306 millimetric water drops,  $Oh \sim 0.0026$ ) [48,63], we consider a range of Weber number below  
307 110 ( $1 \leq We \leq 110$ ) to ensure that the collision outcomes would not fall into the splashing  
308 region. Therefore, a total of 12 cases of  $We$  (i.e.,  $We = 1, 2, 4, 6, 8, 10, 20, 30, 50, 70, 90,$  and  
309 110) are selected (the initial impact velocity  $V_{ini}$  is varied from 0.190 to 2.003 m/s).

310 Also, we considered a broad range of  $Oh$  number ( $0.0013 \leq Oh \leq 0.7869$ ), a total of 10  
311 cases of  $Oh$  (i.e.,  $Oh = 0.0013, 0.0026, 0.0052, 0.0104, 0.0262, 0.0525, 0.1049, 0.2620,$   
312  $0.5246$  and  $0.7869$ ) are selected (the droplet viscosity  $\mu_d$  is varied from 0.0005 to 0.3 N s/m<sup>2</sup>).  
313 Note that such a range of droplet viscosity considered herein corresponds to a range of 0.5 –  
314 300 times the viscosity of a water droplet which covers a range of  $Oh$  of most practical  
315 interest among diverse engineering fields, e.g., gasoline ( $Oh \sim 0.0018$ ), water ( $Oh \sim 0.0026$ ),  
316 ethyl alcohol ( $Oh \sim 0.0063$ ), squalene ( $Oh \sim 0.05$ ), and printable ink ( $Oh \sim 0.1-1.0$ ) with the  
317 given droplet diameter (2 mm) [64,65]. 5 cases of  $\theta_{eqi}$  (i.e.,  $\theta_{eqi} = 20^\circ, 55^\circ, 90^\circ, 125^\circ$  and  
318  $160^\circ$ ) are also selected to cover a wide range of surface wettability from hydrophilic to

319 (super) hydrophobic surfaces.

320 The impact physics on a spherical **target** is practically identical to that on a flat substrate  
321 if a droplet collides onto a sufficiently large **spherical target** which has a diameter 10 times  
322 larger than the droplet (i.e.,  $\Omega \leq 1/10$ ) [38,47]. Note that this assumption has been  
323 experimentally [38] and numerically [40,41] confirmed. Conversely, collision dynamics can  
324 differ greatly on a sufficiently small **spherical target** because a **target** can be fully coated by  
325 the droplet. In this case the typical maximum spreading state cannot be observed and full  
326 coating can usually be observed where  $\Omega \geq 1/1.5$  [39,48]. Therefore, we here examine the  
327 effect of **target** size between those two thresholds ( $1/10 \leq \Omega \leq 1/1.5$ ) and 4 cases of the  
328 droplet-to-**target** size ratio (i.e.,  $\Omega = 1/10, 1/4, 1/3, 1/2$ ) are selected.

329 As a result, a total of 2400 collision cases (12 Weber numbers, 10 Ohnesorge numbers, 5  
330 surface wettabilities and 4 droplet-to-**target** size ratios) are considered in the current study.  
331 This large dataset will also be used to train a deep neural network to formulate a data-driven  
332 prediction model as a non-linear regressor as well as to systematically examine the effects of  
333 4 collision parameters ( $We$ ,  $Oh$ ,  $\theta_{eqi}$  and  $\Omega$ ) on the physical behavior of the spreading time.  
334 For more details of the simulation settings readers can also refer to our previous study  
335 [40,41].

336

## 337 **A. Review of typical spreading dynamics**

338 The schematic diagram in Figure 2 summarizes the different spreading regimes for the  
339 droplet-solid collision system depending on its physical behavior. If a droplet collides onto a  
340 solid surface with sufficiently high inertia, splashing can occur where tiny re-atomized  
341 droplets are generated [12,13]. It has been found that higher  $We$  and lower  $Oh$  normally  
342 promote splashing [59] but the detailed threshold for the onset of splashing can also be  
343 affected by many other collision environments, e.g., surface roughness [63], target curvature

344 [63] and ambient gas pressure [60], etc. Conversely, if a droplet impacts onto a solid surface  
345 with very low inertia compared to surface tension, i.e., at very low Weber number ( $We \leq 1$ ), a  
346 droplet can behave like an elastic ball, sometimes bouncing off a solid surface numerous  
347 times [66]. This region is the so-called elastic regime.

348 Between those two thresholds (i.e., above the elastic threshold and under the splashing  
349 threshold), in general, a droplet spreads over a solid surface and then reaches a maximum  
350 spreading state. Afterward, the droplet can retract and is eventually deposited on a surface (or  
351 can also bounce off a surface depending on surface hydrophobicity) [12,13]. Such a  
352 spreading regime can typically be categorized into the following three sub-regimes depending  
353 on the underlying physical mechanisms: (i) capillary-driven spreading at relatively low  
354 Weber number [41,61], (ii) inertia-driven but capillary-limited (inviscid) at high  $We$  and low  
355  $Oh$  [16,40,62] and (iii) inertia-driven but viscous-limited at high  $We$  and high  $Oh$  [16,40,62].

356 If  $We$  is sufficiently small (i.e.,  $We$  on the order of  $10^0$ ), spreading dynamics is primarily  
357 driven by capillary effects acting on the three-phase triple contact line [61,67,68]. At such a  
358 capillary-driven spreading regime (i.e., regime 1 in Fig.2, also denoted as “CD regime”  
359 hereafter), surface wettability and the associated wetting nature can play more significant  
360 roles in the spreading process rather than inertial effects due to the low Weber number  
361 [18,41]. At a very early stage of contact the apparent contact angle ( $\theta_{ap}$ ) is nearly  $180^\circ$  which  
362 is far from its equilibrium contact angle ( $\theta_{eqi}$ ). Therefore, the capillary force which can be  
363 scaled as  $F_c \sim \sigma R_w (\theta_{ap} - \theta_{eqi})$  (where  $R_w$  is the contact radius) starts to act near the contact line  
364 and drive the spreading process. Note that this capillary effect can make a droplet spread over  
365 a solid surface even if the initial collision velocity is zero and it has also been experimentally  
366 [15] and numerically [41] confirmed that the maximum spreading extent of millimetric  
367 droplets can be larger than the initial droplet diameter in cases of zero impact velocity. In  
368 Fig.2 the CD regime is indicated by the blue region.



369 If  $We$  is sufficiently large [i.e.,  $We \geq O(10^1)$ ] but  $Oh$  is small [i.e.,  $Oh \leq O(10^{-2})$ ], the  
370 spreading process is primarily governed by inertial effects but is terminated by the capillary  
371 limit [16,40,62]. At this inertia-driven but capillary-limited (inviscid) regime (i.e., regime 2 in  
372 Fig.2, also denoted as “IC regime” hereafter), the effects of surface wettability and viscous  
373 dissipation play minor roles in the spreading process, due to the high  $We$  and low  $Oh$   
374 numbers. In other words, a droplet can spread over a surface until the interfacial deformation  
375 is no longer available. The spreading dynamics in the IC regime can also be characterized by  
376 the ejection of a thin liquid sheet (i.e., jetting lamella) at the initial stage [69], and  
377 considerable deformation of the leading edge outer rim can be expected during the  
378 subsequent spreading stage [27,40,70]. The maximum spreading extent can be scaled by the  
379 Weber number, and  $We^{1/4}$  [16,40,62] and  $We^{1/2}$  [29] rules have been shown to work well. In  
380 Fig.2 the IC regime is indicated by the red region.

381 On the other hand, if both  $We$  and  $Oh$  are sufficiently large [i.e.,  $We \geq O(10^1)$  and  $Oh \geq$   
382  $O(10^{-2})$ ], the spreading process is primarily governed by inertial effects but is terminated by  
383 the viscous limit [16,40,62]. At this inertia-driven but viscous-limited spreading regime (i.e.,  
384 regime 3 in Fig.2, also denoted as “IV regime” hereafter), the effect of viscous dissipation  
385 plays a significant role whereas the effect of surface wettability is still negligible due to the  
386 high  $We$  and  $Oh$  numbers. In other words, a droplet can spread over a surface until all the  
387 initial impact (kinetic) energy is dissipated by viscous damping. No lamella ejection is  
388 expected in this viscous regime [19] owing to the strong viscous resistance which hinders the  
389 interfacial deformation. The maximum spreading extent can be scaled by the Reynolds  
390 number and a  $Re^{1/5}$  rule has been found to hold well [16,29,40,62]. In Fig.2 the IV regime is  
391 indicated by the green region.

392 Note that, in the present study, we focus on these three spreading regimes (i.e., CD, IC,  
393 and IV regimes). The other collision regimes (elastic regime and splashing regime) are

394 beyond the current scope due to their different collision phenomena and different area of  
395 interest among the scientific communities.

396 Figure 3 depicts the typical spreading processes of droplets for the three different  
397 spreading regimes summarized in Fig.2 above. The morphological evolutions of spreading  
398 droplets for the CD, IC, and IV regimes are presented in Fig.3(a), (b), and (c), respectively.  
399 Note that the (non-dimensional) advective time scale ( $t_a^*$ ) is used for all cases in Fig.3, since  
400 here we simply focus on describing the typical spreading processes rather than addressing  
401 their detailed physical interpretations. Note also that the collision cases where  $\Omega = 1/10$   
402 which can reasonably be regarded as a flat substrate [38,47] are considered in Fig.3 due to its  
403 generality. As seen in Fig.3(a), the capillary effect acting near the contact line drives the  
404 spreading process for the CD regime. The upper-part of the droplet can nearly maintain its  
405 spherical shape owing to the low Weber number (low impact velocity), whereas a capillary  
406 wave is formed above the contact line due to the local interfacial curvature [see  $t_a^* = 0.34$  in  
407 Fig.3(a)] [18,19,68]. As the capillary waves propagate to the central part of the droplet, the  
408 droplet shows a staircase-like pyramidal structure [18,19,68] without significant interface  
409 deformation ( $0.34 \leq t_a^* \leq 0.50$ ). After the maximum spreading state, the oscillatory motion of  
410 the central part is observed in the vertical direction and then the droplet reaches an  
411 equilibrium state ( $0.50 \leq t_a^* \leq 5.00$ ).

412 In the IC regime, as seen in Fig.3(b), a thin liquid sheet (lamella) is ejected above the  
413 solid surface due to the strong inertial effect overwhelming the surface tension without  
414 significant viscous resistance [see  $t_a^* = 0.25$  in Fig.3(b)]. The droplet rapidly spreads over the  
415 surface and the thin lamella continues consuming liquid mass, forming a thick rim at the  
416 leading edge of the lamella ( $0.80 \leq t_a^* \leq 1.74$ ) [27,40,61,70]. **As the lamella spreads on a  
417 surface, the leading edge of the lamella is detached from the surface due to its strong radial  
418 motion at  $t_a^* = 0.80$ .** After the maximum spreading state, the droplet starts its retraction

419 motion, driven by the capillary effect, to reduce the increased surface energy during the  
420 spreading stage ( $1.74 \leq t_a^* \leq 8.00$ ).

421 In the IV regime, as explained above, no notable lamella ejection is observed [19]. The  
422 interfacial deformation is significantly hindered by the strong viscous damping. After the  
423 maximum spreading state ( $t_a^* = 0.98$ ), the central part of the droplet slightly and slowly rises  
424 again, reaching the equilibrium state, but no meaningful recoiling motion is seen in terms of  
425 its wetted area. Note that all these results showing the evolutions of the droplet morphologies  
426 for the three spreading regimes depicted in Fig.3 are consistent with the experimental  
427 observations of Lin *et al.* [19].

428 Figure 4 quantifies the temporal evolution of the spreading extent characterized by the  
429 non-dimensional spreading diameter  $\beta^*$  ( $\beta^* = \beta/D_d$  where  $\beta$  denotes the arc length of the  
430 droplet in contact with a solid **target**, see the inset in Fig.4) of the droplets for the three  
431 collision cases shown in Fig.3. Note that, for the CD and the IC regimes, detecting the  
432 spreading time with the maximum value of  $\beta^*$  can be straightforward because the droplet  
433 starts its recoiling motion soon after the maximum spreading state (see black solid line and  
434 blue dashed line). The corresponding time for the maximum value of  $\beta^*$  is visually evident.  
435 Conversely, as shown in Fig.3(c), usually no obvious recoiling stage occurs for the IV regime  
436 due to the high viscous resistance (see red dotted line in Fig.4). In this case, detecting the  
437 spreading time can be quite confusing and even a very small disturbance in  $\beta^*$  can lead to a  
438 critical bias for measuring the spreading time. Therefore, to avoid such a complexity, the time  
439 when a droplet attains 95 % of the maximum value of  $\beta^*$  is defined as the spreading time as  
440 marked by three triangles in Fig.4 (see also green arrow). Note that, hereafter, the non-  
441 dimensional forms of the spreading time are denoted by  $\tau_a$  (if the advective time scale is  
442 used),  $\tau_c$  (if the capillary time scale is used) and  $\tau_v$  (if the viscous time scale is used).

443

## 444 **B. Validations**

445 In the above subsection, we addressed the typical spreading dynamics for the three  
446 different spreading regimes. Before we start analyzing the spreading time for each regime in  
447 more detail in this subsection, we validate our simulation method by comparisons with  
448 existing experimental results to check its capability for simulating the droplet collision  
449 phenomena in terms of the spreading time.

450 Figure 5 compares our simulation results with the experimental data of Mitra *et al.* [2]  
451 and Banitabaei and Amirfazli [71] focusing on the collision behavior on spherical targets for  
452 a broad range of We (We = 0.9 – 155.5). First, Fig.5(a) depicts the temporal variation of  $\beta^*$   
453 and the morphological evolution of the droplet for the low Weber number case (We = 0.9).  
454 The insets in Fig.5(a) shows the interfacial shapes captured by the experiment (on the right  
455 side of each panel) [2] and by the current simulation (on the left side of each panel) at three  
456 different time instants ( $t_a^* = 0.24, 0.47, \text{ and } 0.71$ ). As seen, our simulation result shows a  
457 good agreement with the experimental observation. Fig.5(b) depicts the temporal variation of  
458 the non-dimensional film thickness,  $h^*$  [ $h^* = h/D_d$ , where  $h$  is the liquid film thickness  
459 measured on the impact center, see the inset on the lower-left corner in Fig.5(b)] and the  
460 morphological evolutions of the droplet for the high Weber number case (We = 155.5). The  
461 other insets in Fig.5(b) show the interfacial shapes captured by the experiment [71] and by  
462 the current simulation at four different time instants ( $t_a^* = 0.30, 0.60, 1.05 \text{ and } 1.95$ ). Again,  
463 our simulation result shows a good agreement with the experimental observation. Since the  
464 liquid film thickness is one of the most sensitive parameters to the mesh size in this type of  
465 numerical simulations [72], we here present our grid-convergence test result as well in  
466 Fig.5(b). As seen in the dashed gray box, our simulated  $h^*$  almost converges at 32 CPR (cells  
467 per radius) as in our previous study [48,51]. Overall, our simulation result shows an excellent  
468 agreement with the experimental result [71] in terms of both qualitative and quantitative

469 comparisons. Note also that all simulation cases presented in the current study have been  
470 performed with 64 CPR to be on the safe side.

471 In figure 6 we further validate our simulation results focusing on the quantification of the  
472 spreading time for a broad range of We and Oh. Fig.6(a) depicts the non-dimensional  
473 spreading time,  $\tau_a$ , for the low Oh case (Oh = 0.0026 for a water drop). As seen, our  
474 simulation result is consistent with the experimentally measured data of Huang and Chen  
475 [18]. A small deviation can be attributed to the difference of the definition of spreading time  
476 (i.e., we defined the spreading time as the time that a droplet attains 95% of the maximum  
477 spreading extent. See Fig.4 and its explanation). In Fig.6(b), we compare the simulated  $\tau_a$   
478 with the existing numerical result [21] and empirical correlation [19] for the high Oh case  
479 (Oh = 0.62 in the case where the droplet is 240 times the viscosity of a water drop). Our  
480 result again shows an excellent agreement with the existing results [19,21].

481 Further validation test results for drop impact problems are also extensively provided in  
482 Appendix B, which were presented in our previous study. From Figs.5 – 6 and Appendix B,  
483 we can conclude that our simulation methods used in this study can reasonably reproduce the  
484 experimental data for a wide range of collision parameters in the context of both qualitative  
485 and quantitative comparisons. Note that the current numerical framework has been widely  
486 applied to various droplet-solid collision problems and has been thoroughly validated against  
487 many existing experimental data [40,41,48,49,51]. Note also that the impact parameters  
488 considered in our current and previous validation tests reasonably cover the practical  
489 conditions used in the current study ( $0 \leq We \leq 110$ ,  $20^\circ \leq \theta_{eqi} \leq 160^\circ$ ,  $0.0013 \leq Oh \leq 0.7869$   
490 and  $1/10 \leq \Omega \leq 1/2$ ).

491

492 **C. Effects of collision parameters on the spreading time and prediction**  
493 **models**

494 We now analyze the spreading time for the three different spreading regimes addressed  
495 above, i.e., the capillary-driven (CD), the inertia-driven but capillary-limited (IC) and the  
496 inertia-driven but viscous-limited (IV) regimes in more detail and present a prediction model  
497 for each regime. Note that the collision cases for a flat surface ( $\Omega = 1/10$ ) are chosen first for  
498 demonstrating our results owing to its generality. Then we further extend our analysis  
499 considering the effect of the droplet-to-target size ratio ( $\Omega$ ).

500 We first examine the spreading time for the CD regime ( $We \leq 10^1$ ). At this low  $We$   
501 region the spreading dynamics is primarily governed by its wetting nature and the associated  
502 capillary effect where surface wettability plays a dominant role. Therefore, the capillary time  
503 scale,  $t_c^*$ , can be an appropriate time scale for analyzing physical characteristics of the  
504 spreading time in this regime [16,19].

505 Figure 7(a), (b), and (c) depict the effects of  $We$ ,  $\theta_{eqi}$  and  $Oh$  on the spreading profiles,  
506 respectively. As seen in Fig.7(a), the spreading time ( $\tau_c$ ) basically decreases as  $We$  increases  
507 whereas the maximum value of  $\beta^*$  (denoted as  $\beta_{max}^*$  hereafter) increases with  $We$ . This result  
508 is natural because higher spreading velocity can be attained at the high  $We$  cases [19], thus a  
509 shorter spreading time is needed. Note that this is also consistent with the experimental  
510 observation of Lin *et al.* [19]. For the cases shown in Fig.7(a),  $\tau_c$ , where  $We = 10$  ( $\tau_c = 0.69$ ),  
511 is about 21 % shorter compared to that for the case where  $We = 2$  ( $\tau_c = 0.87$ ). In Fig.7(b), as  
512 expected, the dominant effect of the surface wettability is seen. The droplet can spread for a  
513 longer time over the surface as  $\theta_{eqi}$  decreases (i.e., as the surface becomes hydrophilic) and  
514 can attain a larger spreading extent as well owing to the strongly wettable nature of the  
515 hydrophilic surface. This result is also consistent with the existing experimental data [19,43].  
516 For the cases shown in Fig.7(b),  $\tau_c$ , where  $\theta_{eqi} = 20^\circ$  ( $\tau_c = 1.38$ ), is almost double the case  
517 where  $\theta_{eqi} = 160^\circ$  ( $\tau_c = 0.70$ ).

518 It is interesting to observe the effect of  $Oh$  on  $\tau_c$ . As depicted in Fig.7(c), for relatively

519 low Oh cases ( $Oh \leq 0.0104$ , see 4 dashed lines), no meaningful effect of Oh is seen because  
 520 the spreading process is primarily driven by the capillary effect and is also terminated by the  
 521 capillary limit due to the negligible role of the viscous resistance at such low Oh numbers  
 522 [16,40]. Note also that this trend is consistent with the existing experimental observation of  
 523 Lee *et al.* [15] who showed that there was no notable difference of the spreading time  
 524 between a water droplet ( $Oh \sim 0.0026$ ) and a glycerol mixture ( $Oh \sim 0.0263$ , about 10 times  
 525 the viscosity of a water droplet) under the given surface conditions ( $\theta_{eqi} = 52^\circ - 61^\circ$ ) in the  
 526 low We region ( $We < 2.5$ ). Conversely, the spreading profiles start to be affected by Oh as Oh  
 527 further increases above  $Oh \geq 0.0262$  [see solid lines in Fig.7(c)] and the recoiling stages  
 528 disappear for much higher Oh cases ( $Oh \geq 0.1049$ ) owing to the significant viscous damping.  
 529 The interesting point is that no notable difference of  $\tau_c$  can be found even for higher Oh cases  
 530 ( $\tau_c$  is almost constant for the entire range of Oh). We found that this is because Oh primarily  
 531 affects the spreading velocity, not the spreading time, for the higher Oh region. To check the  
 532 effect of Oh on the spreading velocity in more detail, in Fig.7(d) and (e), we plot the non-  
 533 dimensional spreading velocity  $V_s^*$  (defined as  $V_s^* = \beta_{max}^* / \tau_c$ ) and the non-dimensional  
 534 maximum spreading extent  $\beta_{max}^*$  for the cases shown in Fig.7(c), respectively. As seen,  $V_s^*$  is  
 535 nearly constant for the low Oh region (roughly where  $Oh \leq 0.01$ ), whereas it significantly  
 536 decreases as Oh increases in the high Oh region ( $Oh \geq 0.05$ ). Since the effect of Oh on  $\beta_{max}^*$   
 537 (this result in Fig.7(e) is also consistent with the existing experimental result [16]) evidently  
 538 shows exactly the same trend as the effect of Oh on  $V_s^*$ ,  $\tau_c$  can be considered almost  
 539 independent of Oh for the entire range of Oh.

540 It is also interesting to compare the spreading mechanism for this CD regime with the  
 541 retraction mechanism for high-speed impact cases. In fact, both processes (i.e., spreading of  
 542 low-speed impact and retraction of high-speed impact) are presumably based on the same  
 543 physical mechanism, i.e., capillary-driven motion under viscous resistance. In the high-speed

544 impact case, at the beginning of the retraction stage (i.e., right after the maximum spreading  
545 state), the droplet shows a severely deformed interfacial shape and its motion is almost  
546 stopped. Then we begin to see the capillary-driven recoiling motion under viscous resistance,  
547 to reduce its increased surface energy caused by surface deformation during the former  
548 spreading stage [62]. Since the spreading stage in the CD regime is also driven by the  
549 capillary effect under viscous resistance, one can expect that there should essentially and  
550 naturally be consistent physical characteristics between the spreading behavior of the low-  
551 speed impact in the CD regime and the retraction behavior of the high-speed impact cases.  
552 We found that the spreading velocity in the CD regime analyzed in Fig.7(d) demonstrates the  
553 same trend as the retraction characteristics which were experimentally observed by Bartolo *et*  
554 *al.* [62]. They showed that the retraction rate of a droplet is not affected by Oh where  $Oh <$   
555  $0.05$ , whereas it is strongly reduced as Oh increases where  $Oh > 0.05$ . Their result shows an  
556 excellent agreement with our findings described in Figs.7(c) and (d).

557 In Fig.7 above, we observed the obvious effects of We and  $\theta_{eqi}$  on  $\tau_c$ , whereas the effect  
558 of Oh can be negligible. Therefore,  $\tau_c$  in the CD regime can be properly represented by We  
559 and  $\theta_{eqi}$  and **we propose a prediction model:**

560

$$561 \quad \tau_c = (1.66 - 0.31\theta_{eqi}) We^{-0.24} \quad (6)$$

562

563 In figure 8, a total of 600  $\tau_c$  data are plotted with the **prediction model** in Eq.(6). As seen,  
564 all  $\tau_c$  data for a range of  $We \leq 10$  can nearly be collapsed on the single curve (see black solid  
565 line), regardless of Oh. Above the threshold of  $We \sim 10$  (i.e., beyond the CD regime)  $\tau_c$   
566 cannot be properly represented by Eq.(6).

567 We now examine the spreading time for the IC regime [ $We \geq O(10^1)$  and  $Oh \leq O(10^{-2})$ ].  
568 At this high We but low Oh region, the spreading dynamics is primarily dominated by the



569 strong inertial effect but terminated by the capillary limit [16,40,62]. Therefore, the capillary  
570 time scale,  $t_c^*$ , can still be applicable for this regime [16,19].

571 Figure 9(a) depicts the effect of  $We$  on the spreading profiles.  $\tau_c$  first decreases as  $We$   
572 increases for the CD regime (see 5 dashed lines) as shown in Fig.7(a) above, but it increases  
573 again if  $We$  further increases ( $We \geq 30$ ) as the collision dynamics sufficiently enter the IC  
574 regime (see 6 solid lines). This somewhat interesting result can be attributed to the severe  
575 deformation of the leading edge of the lamella and its relaxation phenomena [40]. As the  
576 droplet spreads over the surface the leading edge of the lamella continues deforming. The tip  
577 of the lamella is detached from the surface, and it also continues growing as a rim by  
578 consuming the liquid mass from the central region of the droplet [27,70]. Note that such a  
579 deformed rim plays an important role in determining the maximum wetting area [70] since  
580 the volume of the rim is not small [27] and the maximum wetting area is attained during the  
581 relaxation period of the rim [40]. Therefore, a more deformed shape at higher  $We$  leads to the  
582 longer relaxation time of the rim and eventually the longer spreading time. Fan *et al.* [73] also  
583 experimentally showed that the spreading time of a water droplet on a spherical target first  
584 decreases as  $We$  increases, then it again increases with  $We$  if  $We \geq 36.5$ , showing an  
585 agreement with our results in Fig.9(a). However, the authors think it would be ideal if our  
586 physical interpretation of the underlying mechanism shown in Fig.(b) could also be  
587 confirmed by additional experiments.

588 Fig.9(b) illustrates such a deformation and relaxation process of the rim in more detail.  
589 For the relatively low  $We$  case ( $We = 20$ ), as depicted on the left side of Fig.9(b), the droplet  
590 continues its spreading process until it reaches the maximum spreading state and no  
591 significant deformation of the lamella edge is observed because the spreading dynamics does  
592 not fully enter the IC regime yet. Conversely, for the high  $We$  case where  $We = 110$  [see the  
593 right side of Fig.9(b)], a severe deformation of the rim detached from the surface is clearly

594 captured at  $t_c^* = 0.60\tau_c$  (see black line). Then the rim begins its relaxation to reduce the  
 595 surface energy and eventually reaches the maximum spreading state (see pink line). Note that  
 596 the relaxation period takes quite a long time (about 40 % of  $\tau_c$  in this case) eventually leading  
 597 to the delayed  $\tau_c$ .

598 Fig.9(c) and (d) show the effects of  $\theta_{eqi}$  and Oh on the spreading profiles, respectively.  
 599 As seen, no meaningful effect of  $\theta_{eqi}$  on  $\tau_c$  is observed, because the effect of the surface  
 600 wettability is overwhelmed by the strong inertial effect during most of the spreading stage  
 601 [27,41]. Although the surface wettability plays a non-negligible role in the spreading profiles  
 602 near the maximum spreading state and after  $\tau_c$  (i.e., during the retraction stage) where the  
 603 spreading velocity and the associated inertial effect are at a minimal level, the effect of  $\theta_{eqi}$  on  
 604  $\tau_c$  is almost negligible until the droplet reaches nearly the maximum spreading state. For this  
 605 case  $\tau_c$  can be considered to be a constant value regardless of the surface wettability. The  
 606 effect of Oh on  $\tau_c$  is also not meaningful if Oh is sufficiently small. As seen in Fig.9(d),  $\tau_c$  is  
 607 not affected by Oh if  $Oh < 10^{-2}$  (see 3 solid lines, i.e., at IC regime), whereas  $\tau_c$  decreases as  
 608 Oh increases if  $Oh > 10^{-2}$  (see 3 dashed lines, i.e., beyond the IC regime). This result is also  
 609 consistent with the existing result of Zhu *et al.* [46] who demonstrated that the spreading  
 610 dynamics is independent of Oh for low Oh, whereas it is strongly affected by Oh for high Oh  
 611 under similar We conditions as the present study ( $We \geq 25$ ). Their proposed threshold ( $Oh \sim$   
 612 0.008) is also consistent with the current observation ( $Oh \sim 0.01$ ).

613 In Fig.9 above, we observed the obvious effect of We on  $\tau_c$ , whereas the effects of  $\theta_{eqi}$   
 614 and Oh can be negligible. Therefore,  $\tau_c$  in the IC regime can be properly represented by We  
 615 and **we propose a prediction model:**

616

$$617 \quad \tau_c = 0.31We^{0.18} \quad (7)$$

618

619 In figure 10, a total of 150  $\tau_c$  data are plotted with the **prediction model** in Eq.(7). As  
620 seen, all  $\tau_c$  data for a range of  $We > 30$  can nearly be collapsed on the single curve (see black  
621 solid line) regardless of  $\theta_{eqi}$  and Oh.

622 We now examine the spreading time for the IV regime [ $We \geq O(10^1)$  and  $Oh \geq O(10^{-2})$ ].  
623 At this high We and Oh region the spreading dynamics is primarily dominated by the strong  
624 inertial effect but terminated by the viscous limit [16,40,62]. Therefore, the viscous time  
625 scale,  $t_v^*$ , would be the proper scale in this regime.

626 Figure 11(a), (b), and (c) depict the effects of We,  $\theta_{eqi}$ , and Oh on the spreading profiles,  
627 respectively. As seen in Fig.11(a), the spreading time,  $\tau_v$ , naturally decreases as We increases  
628 due to the higher spreading velocity [19]. The delayed spreading time shown in the IC regime  
629 (caused by the relaxation period of the deformed lamella rim) is not observed in this IV  
630 regime because the interfacial deformation is significantly restricted by the strong viscous  
631 damping. No meaningful effect of  $\theta_{eqi}$  on  $\tau_v$  is seen [see Fig.11(b)] due to its minor role  
632 compared to the strong inertial and viscous effects. Conversely, as expected, the dominant  
633 effect of Oh on  $\tau_v$  is obviously detected in Fig.11(c). Since the spreading stage is terminated  
634 much earlier for higher Oh cases under the given We due to increased viscous resistance (i.e.,  
635 the initial kinetic energy is more quickly dissipated [44]),  $\tau_v$  is significantly reduced for  
636 higher Oh conditions. Note that the effect of Oh on  $\tau_v$  observed in Fig.11(c) is also consistent  
637 with the existing experimental observation [19,44].

638 In Fig.11 above, we observed the obvious effects of We and Oh on  $\tau_v$ , whereas the effect  
639 of  $\theta_{eqi}$  can still be negligible. Therefore,  $\tau_v$  in the IV regime can be properly represented by  
640 We and Oh, and **we propose a prediction model**:

641

$$642 \tau_v = 0.3Oh^{-1.13}We^{-0.22} \quad (8)$$

643

644 In figure 12, a total of 250  $\tau_v$  data are plotted with the **prediction model** in Eq.(8). As  
645 seen, all  $\tau_v$  data for a range of  $We > 30$  can nearly be collapsed on the single curve (see black  
646 solid line), regardless of  $\theta_{eqi}$ .

647

#### 648 **D. Effect of **target** curvature and data-driven prediction model**

649 In the above subsection, we addressed the effects of the three collision parameters ( $We$ ,  
650  $\theta_{eqi}$ , and  $Oh$ ) on the spreading time for the three different spreading regimes (CD, IC, and IV  
651 regimes) and a **prediction model** was presented for each regime for the cases where  $\Omega = 1/10$   
652 (for a flat surface). We now expand our analysis considering the surface curvature which has  
653 been relatively less explored. The effect of the **target** curvature characterized by the droplet-  
654 to-**target** size ratio ( $\Omega$ ) on the spreading time and a new prediction model for the spreading  
655 time which can be applied to the entire range of the 4 collision parameters will be presented  
656 in this subsection.

657 Figure 13(a), (b), and (c) depict the effects of  $\Omega$  on the spreading profiles for the CD, the  
658 IC, and the IV regime, respectively. In the CD regime, as seen in Fig.13(a),  $\tau_c$  increases with  
659  $\Omega$  (on the smaller **target**). This behavior is attributed to the reduced capillary force acting near  
660 the contact line for the smaller **targets**. As described above, at this low  $We$  level, the dominant  
661 force driving the spreading process is the capillary force  $F_c$  [which can be scaled as  $F_c \sim$   
662  $\sigma R_w(\theta_{ap} - \theta_{eqi})$ ] formed at the initial stage of contact. At the instant that a droplet contacts a  
663 solid surface, its apparent contact angle ( $\theta_{ap}$ ) is almost close to  $180^\circ$  and the difference  
664 between the apparent contact angle and the equilibrium contact angle results in the capillary  
665 force  $F_c$  on the contact line. Since such an apparent contact angle at the initial contact stage is  
666 formed at a lower level on the smaller **target** [see  $\theta_{ap2}$  and yellow dashed line in the zoom-in  
667 of the dashed black box, in Fig.13(d)] compared to the bigger **target** (see  $\theta_{ap1}$ ),  $\theta_{ap} - \theta_{eqi}$  and  
668  $F_c$  are reduced on the smaller **targets** eventually leading to lower spreading velocity and

669 longer spreading time. For the cases shown in Fig.13(a),  $\tau_c$  where  $\Omega = 1/2$  ( $\tau_c = 0.99$ ) is about  
670 21 % longer compared to that for the flat surface ( $\Omega = 1/10$ ,  $\tau_c = 0.82$ ).

671 As seen in Fig.13(b), the effect of  $\Omega$  on  $\tau_c$  is apparently observed also in the IC regime,  
672 i.e.,  $\tau_c$  increases on the smaller **targets**. Note that the trend of the effect of  $\Omega$  on  $\tau_c$  in the IC  
673 regime is also consistent with many existing studies [40,46,47] and this behavior is attributed  
674 to the reduced lamella deformation on the smaller **target** [40]. As already shown in Fig.3(b)  
675 above, a thin lamella sheet is ejected at the early stage of spreading. Although the motion of  
676 bulk liquid is primarily dominated by inviscid inertial effects [16,40,62], the dynamics in the  
677 vicinity of the lamella jet is locally but considerably affected by viscous effects [20,69]. Since  
678 the smaller **targets** provide more space in the vertical direction as in an expanding channel  
679 flow for the lamella sheet being ejected [i.e., higher  $\zeta$  is provided on smaller **targets** as  
680 illustrated in the zoom-in of the dashed red box in Fig.13(d)] the local velocity of the radially  
681 expanding lamella jet is reduced on the smaller **targets**. Therefore, the lamella jet develops  
682 less sharply, having a more rounded and bluff shape [40,69]. This allows the droplet to  
683 expend its kinetic energy more efficiently for the spreading itself rather than the rim  
684 deformation detached from the surface eventually leading to the longer spreading time as  
685 well as the longer spreading extent compared to those on the larger **targets** (under the same  
686 kinetic energy level). A more detailed physical mechanism for the reduced lamella  
687 deformation on smaller **targets** can be found in the existing numerical study [40]. For the  
688 cases shown in Fig.13(b),  $\tau_c$ , where  $\Omega = 1/2$  ( $\tau_c = 0.80$ ) is about 45 % longer compared to that  
689 for the flat surface ( $\Omega = 1/10$ ,  $\tau_c = 0.55$ ).

690 The effect of  $\Omega$  on  $\tau_v$  in the IV regime is depicted in Fig.13(c). As seen, no meaningful  
691 effect of  $\Omega$  on  $\tau_v$  is observed for this highly viscous regime. Although the maximum  
692 spreading extent is slightly increased on the smaller **targets** due to the reduced energy  
693 dissipation [40],  $\tau_v$  is almost constant in terms of its practical measurement.

694 In figure 14, we refine the regime map (shown in Fig.2 above) to summarize the major  
695 findings presented so far, including the details of the physical behaviors of the spreading  
696 time. The underlying physical mechanism governing the spreading process, the characteristic  
697 time scale, the effects of various collision parameters on the spreading time and the  
698 **prediction model** (for a flat surface) are also presented for each regime. Note that the effects  
699 of 4 collision parameters, i.e.,  $We$ ,  $\theta_{eqi}$ ,  $Oh$ , and  $\Omega$  are indicated by 4 different markers, i.e.,  
700 circles, squares, triangles and inverted triangles, respectively. If a certain parameter has a  
701 positive (or negative) effect on the spreading time, its effect is indicated by a red (or blue)  
702 marker, whereas an empty marker is used if its effect is negligible. For example, if the  
703 spreading time increases with  $We$ , the effect of  $We$  is marked by a filled red circle.  
704 Conversely, the effect of  $We$  is marked by a filled blue circle if the spreading time decreases  
705 as  $We$  increases.

706 Fig.14 highlights the complex nature of the spreading time owing to the different  
707 physical mechanism for each regime. The effects of the impact parameters ( $We$ ,  $\theta_{eqi}$ ,  $Oh$  and  
708  $\Omega$ ) also play different roles. For instance, the effect of  $We$  is positively related to the  
709 spreading time for the CD and the IV regime, whereas it is negatively related to the spreading  
710 time for the IC regime. In particular, none of the 4 impact parameters shows a consistent  
711 effect across the three spreading regimes, which highlights the significant nonlinearity and  
712 complexity of the spreading time. The characteristic time scales are also different.

713 Therefore, formulating a single correlation for the spreading time as a broad cross-over  
714 across the three different spreading regimes is quite difficult since it should cover all the  
715 different physical mechanisms, different characteristic time scales, and different effects of the  
716 collision parameters. In addition, if the effect of the **target** curvature (i.e., the effect of  $\Omega$ ) on  
717 the spreading time were to be considered together, the problem would be much more  
718 complicated. Rather than formulating a single correlation, therefore, we consider here a data-

719 driven approach to model such complex and non-linear behavior of the spreading time across  
720 all the spreading regimes.

721 Recently, data-driven approaches have been broadly applied to model complicated fluid  
722 phenomena such as turbulent flows [74] or multiphase flow systems [75]. For droplet impact  
723 problems as well, the maximum spreading extent [41], the splashing threshold [76], and the  
724 lamella area [77] have successfully been modeled using data-driven techniques, based on  
725 their powerful ability to correlate non-linear relations among large datasets and reduce the  
726 level of complexity.

727 The spreading time can basically be modeled as a function of 4 impact parameters as  
728 follows:

729

$$730 \quad \tau_a = f(\text{We}, \text{Oh}, \theta_{\text{eqi}}, \Omega) \quad (9)$$

731

732 Here, the advective time scale is applied for our data-driven prediction model, in order to  
733 treat our dataset in a consistent manner.  $f$  is the non-linear and complicated (unknown)  
734 function between inputs (4 impact parameters) and output ( $\tau_a$ ) data which is now modeled by  
735 using an artificial intelligence technique. The multilayer neural network, also called the  
736 multilayer perceptron (MLP) [78], is utilized as a nonlinear regressor to model the function  $f$ .  
737 Figure 15 illustrates the schematic diagram of the typical MLP structure. The MLP consists of  
738 the input layer (marked by red nodes), the multiple hidden layers (marked by green nodes)  
739 and the output layer (marked by blue nodes). Each layer usually consists of a number of  
740 nodes (also called neurons), whereas the last output layer has only one output node. The 4  
741 input features ( $\text{We}$ ,  $\text{Oh}$ ,  $\theta_{\text{eqi}}$  and  $\Omega$ ) are provided from the input layer to the first hidden layer  
742 and then linear combinations of the input features are calculated on each node. Such linear  
743 combinations are nonlinearized by using an activation function and then are delivered to the

744 next hidden layer. Such an operation is called a feedforward procedure and is applied to all  
745 the subsequent layers. The last output layer has no nonlinearization operation and provides  
746 the final output value.

747 A total of 2400 impact cases (12 Weber numbers, 10 Ohnesorge numbers, 5 surface  
748 wettabilities, and 4 droplet-to-**target** size ratios) are utilized to set the dataset. The dataset is  
749 randomly split into 3 parts: the training dataset (70 %, 1680 data points), the validation  
750 dataset (15 %, 360 data points) and the test dataset (15 %, 360 data points). The training  
751 dataset and the test dataset are used to train our MLP model and finally test the accuracy of  
752 the trained model, respectively, whereas the validation dataset is utilized to check if  
753 overfitting occurs during the training process. More detailed information on our MLP  
754 modeling and its training procedure can be found in the **Appendix C**.

755 Figure 16 compares the spreading time predicted by our data-driven model with the true  
756 values (measured values from our numerical simulations). 360 data points from the test  
757 dataset are plotted for comparison (see black circles). As can be seen,  $\tau_a$  predicted by our  
758 MLP model demonstrates a good agreement with the true dataset, showing that the mean  
759 square error (MSE) is on the order of  $O(10^{-4})$  ( $MSE = 5.23 \times 10^{-4}$ ). Note that, except for only  
760 a few cases, all the tested cases fall inside a deviation range of  $\pm 15\%$ . Note that all the test  
761 data samples shown in Fig.16 have not been used for the training process of our MLP model.  
762 To the best of our knowledge, our prediction model is the first data-driven model for the  
763 spreading time of the **droplet collision system which can be applied for a curved spherical**  
764 **target**. As one of the most universal models, the current model can cover a very broad range  
765 of impact parameters across not only the three spreading regimes (i.e., CD, IC, IV regimes  
766 and the transition area among them as well), but also a wide range of droplet-to-**target** size  
767 ratio (from a flat substrate to a small **spherical target**).

768 **Last but not least, the authors would like to clarify that there is no physics in the current**



769 data-driven prediction model, which can indeed be understood as providing both pros and  
770 cons [75]. The fact that such a data-driven approach is not fully based on a physical  
771 background might be a reason for which it has been less attractive to some scientific  
772 communities compared to conventional approaches supported by strong physical principles  
773 [79,80]. However, both approaches share identical goals, i.e., modeling complicated  
774 phenomena which usually need to consider many multi-dimensional variables [80,81]. The  
775 advantages of data-driven approaches can also be that users would not need to consider  
776 physics models alone for those complex system because data-driven models basically don't  
777 rely on constraints attributed to physics [75]. This characteristic allows them to work as a  
778 useful non-linear regressor. For example, the current data-driven prediction model can predict  
779 the spreading time even for transition regimes marked in the gray zones in Fig.14, which is  
780 apparently very difficult to predict using Eqs. 6 – 8 above due to their non-linear nature. This  
781 clearly shows the advantage of data-driven approaches at least in the context of engineering  
782 applications and practical usefulness.

783

## 784 **IV. CONCLUSION**

785

786 In this study we quantitatively and systematically investigate the spreading time of droplet  
787 impact onto a spherical target for a wide range of impact parameters ( $0 \leq We \leq 110$ ,  $20^\circ \leq$   
788  $\theta_{eqi} \leq 160^\circ$ ,  $0.0013 \leq Oh \leq 0.7869$  and  $1/10 \leq \Omega \leq 1/2$ ). A total of 2400 collision cases are  
789 simulated and are used to better understand the physical behavior of the spreading time. This  
790 large simulation dataset is also used for training a data-driven prediction model as well as for  
791 the derivation of prediction models.

792 For the three different spreading regimes, i.e., the capillary-driven (CD), the inertia-

793 driven but capillary-limited (IC) and the inertia-driven but viscous-limited (IV) regimes, the  
794 effects of the impact parameters on the spreading time are analyzed in detail. Not only the  
795 spreading time, but also proper time scales, dominant impact parameters and associated  
796 physical behaviors all significantly and non-linearly change across the three spreading  
797 regimes. The spreading time is primarily dominated by the  $We$  and  $\theta_{eqi}$  in the CD regime  
798 whereas only the Weber number plays a meaningful role in the IC regime. In the IV regime it  
799 is mainly affected by  $We$  and  $Oh$ . An improved prediction model is also presented for each  
800 regime. To the best of our knowledge, these proposed prediction models (Eqs. 6-8) are the  
801 first models for the spreading time using only the controllable independent variables (e.g.,  
802  $We$ ,  $Oh$  and  $\theta_{eqi}$ ) in explicit form which can provide more straightforward solutions compared  
803 to the existing models [18-21,44,45].

804 The effect of target curvature on the spreading time is also analyzed in detail for the  
805 three different spreading regimes, showing complicated trends due to its non-linear nature.  
806 Finally, a data-driven prediction model is proposed to predict the spreading time broadly  
807 across the three different spreading regimes. Our proposed data-driven model shows good  
808 prediction capability for the full ranges of impact parameters considered in the present study  
809 and also shows a good agreement with our simulation dataset.

810 The limitation of the current study is as follows: (i) As in the existing models, prediction  
811 models (Eqs. 6-8) are still not derived from physical background. Further efforts are needed  
812 to combine “physics-based models” which could be helpful in understanding such  
813 complicated behavior within the existing empirical results. (ii) Users need to be careful in  
814 using the proposed data-driven model. Although our numerical methods have thoroughly  
815 been validated, the number of current data samples (2400 cases) is still insufficient to model  
816 the spreading time for the entire spreading regime compared to other common data-driven  
817 models trained using “big-data”. Our numerical data used for the training are also confined to

818 the current impact conditions ( $0 \leq We \leq 110$ ,  $20^\circ \leq \theta_{\text{eqi}} \leq 160^\circ$ ,  $0.0013 \leq Oh \leq 0.7869$  and  
819  $1/10 \leq \Omega \leq 1/2$ ). Broader ranges of impact parameters, and more precise and abundant data  
820 samples can improve the applicability and accuracy of the current model. (iii) While the  
821 current axi-symmetric simulation code is sufficiently validated, full three-dimensional  
822 simulations are still essential to better understand those complicated physical phenomena. In  
823 particular, impact dynamics at high  $We$  and low  $Oh$  where the liquid sheets and rim can be  
824 highly deformed still need to be captured more precisely. We are currently working on these  
825 issues.

826

## 827 **APPENDIX A: Details of the dynamic contact angle**

### 828 **modeling**

829

830 The dynamic contact angle  $\theta_{\text{dyn}}$  is basically modeled as a function of the equilibrium  
831 contact angle and the velocity of the contact line, as in well-known previous numerical  
832 studies on drop impact problems [82,83]. In the present study, we use the model of Yokoi *et*  
833 *al.* [83]:

834

$$835 \quad \theta_{\text{dyn}}(U_{\text{CL}}) = \begin{cases} \min \left[ \theta_{\text{eqi}} + \left( \frac{\text{Ca}}{q_1} \right)^{1/3}, \theta_{\text{mda}} \right], & \text{if } U_{\text{CL}} \geq 0 \text{ (for spreading)} \\ \max \left[ \theta_{\text{eqi}} + \left( \frac{\text{Ca}}{q_2} \right)^{1/3}, \theta_{\text{mdr}} \right], & \text{if } U_{\text{CL}} \leq 0 \text{ (for receding)}. \end{cases} \quad (\text{A1})$$

836

837  $\text{Ca}$  is the capillary number ( $\text{Ca} = \mu U_{\text{CL}} / \sigma$ ), where  $U_{\text{CL}}$  is the velocity of the contact line.

838 Contact angle hysteresis is represented by the difference between the allowable minimum

839  $(\theta_{\text{mdr}})$  and maximum  $(\theta_{\text{mda}})$  contact angles, and the dynamic contact angle  $(\theta_{\text{dyn}})$  can always  
840 be maintained between  $\theta_{\text{mdr}}$  and  $\theta_{\text{mda}}$ .  $q_1$  and  $q_2$  are experimentally measured constants, and  
841 the same values as in Yokoi *et al.* [83] ( $q_1 = 9.0 \times 10^{-9}$  and  $q_2 = 9.0 \times 10^{-8}$ ) are applied to the  
842 current study.

843

## 844 **APPENDIX B: Validation tests in our previous studies**

845

846 We here introduce our validation test results presented in our previous studies. Figure  
847 17(a) compares the maximum spreading extent  $\beta^*_{\text{max}}$  computed by our simulation with Mao  
848 *et al.* [25]’s semi-empirical model which is well-known as one of the most accurate models  
849 that can be applied for a wide range of drop viscosity [84].  $\beta^*_{\text{max}}$  shows generally good  
850 agreement with the existing model of Mao *et al.* [25] for a wide range of We number ( $30 \leq$   
851  $We \leq 90$ ) and Oh number ( $0.0013 \leq Oh \leq 0.7869$ ). Note that a discrepancy shown at the very  
852 low Oh region ( $Oh \leq 0.0026$ ) is attributed to the limitation of shape approximation in Mao *et*  
853 *al.*’s model [25], which overestimates  $\beta^*_{\text{max}}$  if the viscosity is very low and the surface tension  
854 force plays an important role [25,84]. Therefore, in figure 17(b), we compare our simulated  
855  $\beta^*_{\text{max}}$  again with the well-known viscous-free scaling law proposed by Clanet *et al.* [16]. As  
856 can be seen, for cases with very low Oh number ( $Oh = 0.0026$ ), our simulation result shows  
857 an excellent agreement with the existing scaling law [16].

858 In figure 17(c), we further compare our simulated time-dependent non-dimensional  
859 spreading diameter  $\beta^*$  with three existing experimental results to see if our numerical  
860 framework can simulate the impact phenomena well on spherical targets. The solid lines in  
861 Fig. 17(c) depict the simulation results, whereas the red squares, blue circles, and black  
862 crosses show the experimental results from Mitra *et al.* [2], Liu *et al.* [38], and Khurana *et al.*  
863 [39], respectively. Our simulation results also show good agreement with the existing

864 experimental observations in the literature, in the context of dynamic spreading  
 865 characteristics. Overall, we concluded that our simulation framework can simulate the drop  
 866 impact phenomena on both flat and spherical targets well for a wide range of collision  
 867 parameters. Note again that these validation tests shown in figure 17 are not new tests, but  
 868 were already presented in our previous study [40].

869

## 870 **APPENDIX C: Details of MLP training**

871

872 The output value on the  $n^{\text{th}}$  node in the  $m^{\text{th}}$  layer is:

873

$$874 \quad a_n^m = g \left( \sum_{k=1}^{N^{m-1}} w_{nk}^m a_k^{m-1} + b_n^m \right) \quad (\text{C1})$$

875

876 Here,  $N$  stands for the number of nodes of each layer. The function  $g$  denotes the nonlinear  
 877 activation function.  $w_{nk}$  is the weight between the  $k^{\text{th}}$  node of the previous layer and the  $n^{\text{th}}$   
 878 node of the current layer whereas  $b$  is the bias.

879 The weights ( $w$ ) and biases ( $b$ ) are adjustable coefficients and are first initialized as  
 880 random variables and zero, respectively.  $w$  and  $b$  are continuously updated during the training  
 881 process, minimizing the loss function based on the back-propagation algorithm [85]. In the  
 882 current study, the mean square error (MSE) is used as a loss function:

883

$$884 \quad \text{MSE} = \frac{1}{M} \sum_{k=1}^M (\tau_a - \tau_{a(p)})^2 \quad (\text{C2})$$

885

886 where  $M$  is the number of data points considered and  $\tau_{a(p)}$  is the predicted value of the

887 spreading time using the trained MLP model.

888 Three hyperparameters (i.e., the activation function, the number of nodes at each hidden  
889 layer and the number of hidden layers) can usually be selected by the user. We chose the  
890 common rectified linear unit function (generally called ReLU) as our activation function  
891 owing to its well-known capability for deep neural networks [86]. The ReLU can be written  
892 as:

$$894 \quad g(x) = \text{ReLU}(x) = \max(x, 0) \quad (\text{C3})$$

895  
896 Two other hyperparameters are set by manual search because the current dataset is relatively  
897 very simple. Finally, a  $4 \times 30$  (4 hidden layers and 30 neurons in each hidden layer)  
898 architecture is chosen as the MLP network. The ADAM optimization procedure [87,88] is  
899 used for the MLP training and the computational implementation for the MLP training is  
900 performed using the open-source libraries Keras [89] and TensorFlow [90]. For more details  
901 on the deep learning architecture and its training techniques readers can refer to Nielsen [91].

902 The training of our MLP model is carried out until the validation MSE (measured from  
903 the validation dataset) reaches a steady state. After 3300 training epochs the validation MSE  
904 converges to a steady state of about  $4.62 \times 10^{-4}$  (see Fig.18).

905

906

907

908

909

910

911

## 912 **DECLARATIONS**

913

### 914 **Ethical Approval**

915 Not applicable.

916

### 917 **Conflict of interest**

918 The authors declare that they have no conflict of interest.

919

### 920 **Authors' contributions**

921 Ikroh Yoon led conceptualization, data curation, formal analysis, investigation, validation,  
922 visualization, and writing (draft). Seungwon Shin led funding acquisition, methodology,  
923 resources, and software, and supported conceptualization, data curation, formal analysis,  
924 investigation, validation, visualization, and writing (draft). Damir Juric and Jalel Chergui  
925 supported conceptualization, data curation, formal analysis, funding acquisition,  
926 investigation, methodology, resources, software, validation, visualization, and writing (draft).  
927 All authors equally contributed to reviewing/editing the manuscript.

928

### 929 **Funding**

930 This work was supported by the National Research Foundation of Korea (NRF) grant funded  
931 by the Korea government (MSIT) (RS-2023-00244322) and support through computing time  
932 at the Institut du Developpement et des Ressources en Informatique Scientifique (IDRIS) of  
933 the Centre National de la Recherche Scientifique (CNRS), coordinated by GENCI (Grand  
934 Equipement National de Calcul Intensif) Grant 2023 A0142B06721.

935

## 936 **Data availability**

937 The data that support the findings of this study are available from the corresponding author, I.  
938 Yoon, upon reasonable request.

939

940

941

942

943

## 944 **References**

945 1. D. Khojasteh, N. M. Kazerooni, and M. Marengo, "A review of liquid droplet  
946 impacting onto solid spherical particles: A physical pathway to encapsulation  
947 mechanisms," *J. Ind. Eng. Chem.* **71**, 50–64 (2019).

948

949 2. S. Mitra, G. M. Evans, E. Doroodchi, V. Pareek, and J. B. Joshi, "Interactions in  
950 droplet and particle system of near unity size ratio," *Chem. Eng. Sci.* **170**, 154–175  
951 (2017).

952

953 3. J. D. Oxley, "5 - Spray cooling and spray chilling for food ingredient and  
954 nutraceutical encapsulation," *Encapsulation Technologies and Delivery Systems for  
955 Food Ingredients and Nutraceuticals*, Woodhead Publishing, 110-130 (2012).

956

957 4. V. Nedovic, A. Kalusevic, V. Manojlovic, S. Levic and B. Bugarski, "An overview of  
958 encapsulation technologies for food applications," *Procedia Food Sci.* **1**, 1806-1815  
959 (2011).



- 960  
961 5. T. Chien and H. Chu, "Removal of SO<sub>2</sub> and NO from flue gas by wet scrubbing using  
962 an aqueous NaClO<sub>2</sub> solution," *J. Hazard. Mater.* **80** (1–3), 43-57 (2000).
- 963  
964 6. E. Teunou, and D. Poncelet, "Batch and continuous fluid bed coating – review and  
965 state of the art," *Journal of Food Engineering*, **53** (4), 325-340 (2002).
- 966  
967 7. A. Kundu, K. D. P. Nigam and R. P. Verma, "Catalyst wetting characteristics in  
968 trickle-bed reactors," *AIChE J.* **49** (9), 2253-2263 (2003).
- 969  
970 8. B. Moon, N. Abbasi, S. G. Jones, D. K. Hwang and S. S. H. Tsai, "Water-in-Water  
971 Droplets by Passive Microfluidic Flow Focusing," *Anal. Chem.* **88** (7), 3982-3989  
972 (2016).
- 973  
974 9. D. A. Bolleddula, A. Berchielli and A. Aliseda, "Impact of a heterogeneous liquid  
975 droplet on a dry surface: Application to the pharmaceutical industry," *Advances in  
976 Colloid and Interface Science*, **159** (2) 144-159 (2010).
- 977  
978 10. G. Charalampous and Y. Hardalupas, "Collisions of droplets on spherical particles,"  
979 *Phys. Fluids* **29**, 103305 (2017).
- 980  
981 11. S. Sohrabi, N. kassir, and M. K. Moraveji, "Retracted Article: Droplet microfluidics:  
982 fundamentals and its advanced applications," *RSC Adv.* **10** (46) 27560-27574 (2020).
- 983  
984 12. C. Josserand and S. T. Thoroddsen, "Drop impact on a solid surface," *Annu. Rev.  
985 Fluid Mech.* **48**, 365–391 (2016).
- 986  
987 13. A. L. Yarin, "Drop Impact Dynamics: Splashing, Spreading, Receding, Bouncing, ...,"  
988 *Annu. Rev. Fluid Mech.* **38**, 159 (2006).
- 989

- 990 14. C. Antonini, A. Amirfazli, and M. Marengo, "Drop impact and wettability: From  
991 hydrophilic to superhydrophobic surfaces," *Phys. Fluids* **24**, 102104 (2012).
- 992  
993 15. J. B. Lee, N. Laan, K. G. De Bruin, G. Skantzaris, N. Shahidzadeh, D. Derome, J.  
994 Carmeliet, and C. Bonn, "Universal rescaling of drop impact on smooth and rough  
995 surfaces," *J. Fluid Mech.* **786**, R4 (2016).
- 996  
997 16. C. Clanet, C. Béguin, D. Richard, and D. Quéré, "Maximal deformation of an  
998 impacting drop," *J. Fluid Mech.* **517**, 199–208 (2004).
- 999  
1000 17. S. Wildeman, C. Visser, C. Sun, and D. Lohse, "On the spreading of impacting  
1001 drops," *J. Fluid Mech.* **805**, 636–655 (2016).
- 1002  
1003 18. H. Huang and X. Chen, "Energetic analysis of drop's maximum spreading on solid  
1004 surface with low impact speed", *Phys. Fluids* **30**, 022106 (2018).
- 1005  
1006 19. S. Lin, B. Zhao, S. Zou, J. Guo, Z. Wei, and L. Chen, "Impact of viscous droplets on  
1007 different wettable surfaces: Impact phenomena, the maximum spreading factor,  
1008 spreading time and post-impact oscillation," *Journal of Colloid and Interface Science*,  
1009 **516**, 86-97 (2018).
- 1010  
1011 20. Y. T. Aksoy, P. Eneren, E. Koos, and M. R. Vetrano, "Spreading of a droplet  
1012 impacting on a smooth flat surface: How liquid viscosity influences the maximum  
1013 spreading time and spreading ratio," *Phys. Fluids.* **34**, 042106 (2022).
- 1014  
1015 21. Du, X. Wang, Y. Li, Q. Min, and X. Wu, "Analytical Consideration for the Maximum  
1016 Spreading Factor of Liquid Droplet Impact on a Smooth Solid Surface," *Langmuir*  
1017 **37**, 7582-7590 (2021).
- 1018

- 1019 22. J. Ancheyta, “Modeling and Simulation of Catalytic Reactors for Petroleum  
1020 Refining,” Wiley, (2011).
- 1021  
1022 23. S. Chandra and C. T. Avedisian, “On the collision of a droplet with a solid surface,”  
1023 Proc. R. Soc. London A **432**, 13 (1991).
- 1024  
1025 24. M. Pasandideh-Fard, Y. Qiao, S. Chandra, and J. Mostaghimi, “Capillary effects  
1026 during droplet impact on a solid surface,” Phys. Fluids **8**, 650 (1996).
- 1027  
1028 25. T. Mao, D. Kuhn, and H. Tran, “Spread and rebound of liquid droplets upon impact  
1029 on flat surfaces,” AIChE J. **43**, 2169–2179 (1997).
- 1030  
1031 26. C. Ukiwe and D. Y. Kwok, “On the maximum spreading diameter of impacting  
1032 droplets on well-prepared solid surfaces,” Langmuir **21**, 2, 666–673 (2005).
- 1033  
1034 27. I. V. Roisman, “Inertia dominated drop collisions. II. An analytical solution of the  
1035 Navier–Stokes’s equations for a spreading viscous film,” Phys. Fluids **21**, 052104  
1036 (2009).
- 1037  
1038 28. N. Laan, K. G. de Bruin, D. Bartolo, C. Josserand, and D. Bonn, "Maximum  
1039 Diameter of Impacting Liquid Droplets," Phys. Rev. Applied **2**, 044018 (2014).
- 1040  
1041 29. J. Eggers, M. A. Fontelos, C. Josserand, and S. Zaleski, “Drop dynamics after impact  
1042 on a solid wall: Theory and simulations,” Phys. Fluids **22**, 062101 (2010).
- 1043  
1044 30. I. V. Roisman, R. Rioboo, and C. Tropea, “Normal impact of a liquid drop on a dry  
1045 surface: Model for spreading and receding,” Proc. R. Soc. Lond. A. **458**, 1411–1430  
1046 (2002).
- 1047

- 1048 31. S. Bakshi, I. V. Roisman, and C. Tropea, “Investigations on the impact of a drop onto  
1049 a small spherical target,” *Phys. Fluids* **19**, 032102 (2007).
- 1050 32. I. Malgarinos, N. Nikolopoulos, and M. Gavaises, “A numerical study on droplet-  
1051 particle collision dynamics,” *Int. J. Heat Fluid Flow* **61**, 499–509 (2016).
- 1052  
1053 33. I. Malgarinos, N. Nikolopoulos, and M. Gavaises, "Numerical investigation of heavy  
1054 fuel droplet-particle collisions in the injection zone of a Fluid Catalytic Cracking  
1055 reactor, part II: 3D simulations," *Fuel Processing Technology* **156**, 43-53 (2017).
- 1056  
1057 34. D. Zhang, K. Papadikis, and S. Gu, “Investigations on the Droplet Impact onto a  
1058 Spherical Surface with a High Density Ratio Multi-Relaxation Time Lattice-  
1059 Boltzmann Model,” *Communications in Computational Physics* **16** (4), 892-912  
1060 (2014).
- 1061  
1062 35. D. Zhang, K. Papadikis, and S. Gu, “Application of a high density ratio lattice-  
1063 Boltzmann model for the droplet impingement on flat and spherical surfaces,” *Int. J.*  
1064 *Therm. Sci.* **84**, 75–85 (2014).
- 1065  
1066 36. G. Liang, Y. Guo, X. Mu, S. Shen, "Experimental investigation of a drop impacting  
1067 on wetted spheres," *Experimental Thermal and Fluid Science* **55**, 150-157 (2014).
- 1068  
1069 37. S. Mitra, T. B. T. Nguyen, E. Doroodchi, V. Pareek, J. B. Joshi, and G. M. Evans, “On  
1070 wetting characteristics of droplet on a spherical particle in film boiling regime,”  
1071 *Chem. Eng. Sci.* **149**, 181–203 (2016).
- 1072  
1073 38. X. Liu, X. Zhang, and J. Min, “Maximum spreading of droplets impacting spherical  
1074 surfaces,” *Phys. Fluids*. **31**, 092102 (2019).
- 1075  
1076

- 1077 39. G. Khurana, N. Sahoo, and P. Dhar, "Phenomenology of droplet collision  
1078 hydrodynamics on wetting and non-wetting spheres," *Phys. Fluids* **31**, 072003  
1079 (2019).
- 1080  
1081 40. I. Yoon and S. Shin, "Maximal spreading of droplet during collision on particle:  
1082 effects of liquid viscosity and surface curvature," *Phys. Fluids* **33**, 083310 (2021).
- 1083  
1084 41. I. Yoon, J. Chergui, D. Juric, and S. Shin, "Maximum spreading of droplet-particle  
1085 collision covering a low Weber number regime and data-driven prediction model,"  
1086 *Phys. Fluids* **34**, 102109 (2022).
- 1087  
1088 42. D. Richard, C. Clanet, and D. Quéré, "Contact time of a bouncing drop," *Nature* **417**,  
1089 **811** (2002).
- 1090  
1091 43. D. C. Vadillo, A. Soucemarianadin, C. Delattre, and D. C. D. Roux, "Dynamic contact  
1092 angle effects onto the maximum drop impact spreading on solid surfaces," *Phys.*  
1093 *Fluids* **21**, 122002 (2009).
- 1094  
1095 44. J. B. Lee, D. Derome, R. Guyer, and J. Carmeliet, "Modeling the Maximum  
1096 Spreading of Liquid Droplets Impacting Wetting and Nonwetting Surfaces,"  
1097 *Langmuir* **32**, 1299-1308 (2016).
- 1098  
1099 45. F. Wang, L. Yang, L. Wang, Y. Zhu, and T. Fang, "Maximum Spread of Droplet  
1100 Impacting onto Solid Surfaces with Different Wettabilities: Adopting a Rim-Lamella  
1101 Shape," *Langmuir* **35**, 3204-3214 (2019).
- 1102  
1103 46. Y. Zhu, H. Liu, K. Mu, P. Gao, H. Ding, and X. Lu, "Dynamics of drop impact onto a  
1104 solid sphere: Spreading and retraction." *J. Fluid Mech.* **824**, R3 (2017).
- 1105

- 1106 47. X. Liu, J. Min, X. Zhang, Z. Hu, and X. Wu, "Supercooled water droplet impacting-  
1107 freezing behaviors on cold superhydrophobic spheres," *Int. J. Multiph. Flow* **141**,  
1108 103675 (2021).
- 1109 48. I. Yoon and S. Shin, "Direct numerical simulation of droplet collision with stationary  
1110 spherical particle: A comprehensive map of outcomes," *Int. J. Multiph. Flow* **135**,  
1111 103503 (2021).
- 1112 49. I. Yoon, C. Ha, C. Lee, and S. Shin, "Promoting rebound from droplet impact on a  
1113 spherical particle: Experimental and numerical study," *Phys. Fluids* **34**, 103302  
1114 (2022).
- 1115 50. J. Han, W. Kim, C. Bae, D. Lee, S. Shin, Y. Nam, and C. Lee, "Contact time on  
1116 curved superhydrophobic surfaces," *Phys. Rev. E* **101**, 043108 (2020).
- 1117 51. I. Yoon, J. Chergui, D. Juric, and S. Shin, "Adaptive mesh axi-symmetric simulation  
1118 of droplet impact with a spherical particle in mid-air," *Int. J. Multiph. Flow* **155**,  
1119 104193 (2022).
- 1120 52. S. Shin, J. Chergui, and D. Juric, "A solver for massively parallel direct numerical  
1121 simulation of three-dimensional multiphase flows," *J. Mech. Sci. Technol.* **31**, 1739–  
1122 1751 (2017).
- 1123 53. J.U. Brackbill, D.B Kothe and C. Zemach, "A continuum method for modeling  
1124 surface tension," *J. Comput. Phys.* **100** (2), 335-354 (1992).
- 1125 54. S. Unverdi, and G. Tryggvason, "A front-tracking method for viscous,  
1126 incompressible, multi-fluid flows," *J. Comput. Phys.* **100**, 25–37 (1992).
- 1127  
1128  
1129  
1130  
1131  
1132  
1133  
1134

- 1135 55. S. Shin, and D. Juric, "Modeling three-dimensional multiphase flow using a level  
1136 contour reconstruction method for front tracking without connectivity," *J. Comput.*  
1137 *Phys.* **180**, 427–470 (2002).
- 1138 56. S. Shin and D. Juric, "A hybrid interface method for three-dimensional multiphase  
1139 flows based on front tracking and level set techniques," *Int. J. Numer. Meth. Fluids*  
1140 **60**, 753–778 (2009).
- 1141 57. S. Shin, J. Chergui, and D. Juric, "Direct simulation of multiphase flows with  
1142 modeling of dynamic interface contact," *Theor. Comput. Fluid Dyn.* **32**, 655–687  
1143 (2018).
- 1144 58. S. Osher and J. Sethian, "Fronts propagating with curvature-dependent speed:  
1145 Algorithms based on Hamilton-Jacobi formulations," *J. Comput. Phys.* **79**, 12–49  
1146 (1988).
- 1147 59. C. Mundo, M. Sommerfeld, and C. Tropea, "Droplet-wall collisions: experimental  
1148 studies of the deformation and breakup process," *Int. J. Multiph. Flow* **21**(2), 151–  
1149 173 (1995).
- 1150 60. L. Xu, W. W. Zhang, and S. R. Nagel, "Drop Splashing on a Dry Smooth Surface,"  
1151 *Phys. Rev. Lett.* **94** (18), 184505 (2005).
- 1152 61. I. V. Roisman, E. Berberović, and C. Tropea, "Inertia dominated drop collisions. I. On  
1153 the universal flow in the lamella," *Phys. Fluids* **21**, 052103 (2009).
- 1154 62. D. Bartolo, C. Josserand, and D. Bonn, "Retraction dynamics of aqueous drops upon  
1155 impact on non-wetting surfaces," *J. Fluid Mech.* **545**, 329–338 (2005).
- 1156  
1157  
1158  
1159  
1160  
1161  
1162  
1163

- 1164 63. Y. Hardalupas, A. M. K. P. Taylor and J. H. Wilkins, “Experimental investigation of  
1165 sub-millimetre droplet impingement on to spherical surfaces,” *Int. J. Heat Fluid Flow*  
1166 **20** (5), 477–485 (1999).
- 1167  
1168 64. G. H. McKinley and M. Renardy, “Wolfgang von Ohnesorge,” *Phys. Fluids*. **23**,  
1169 127101 (2011).
- 1170  
1171 65. B. R. Munson, D. F. Young, and T. H. Okiishi, *Fundamentals of Fluid Mechanics*, 5th  
1172 ed. (John Wiley and Sons, New York, 2006)
- 1173  
1174 66. A. Biance, F. Chevy, C. Clanet, G. Lagubeau, and D. Quéré, “On the elasticity of an  
1175 inertial liquid shock,” *J. Fluid Mech.* **554** (1), 47–66 (2006).
- 1176  
1177 67. J. Du, N. T. Chamakos, A. G. Papanthasiou, and Q. Min, "Initial spreading dynamics  
1178 of a liquid droplet: The effects of wettability, liquid properties, and substrate  
1179 topography,” *Phys. Fluids*. **33**, 042118 (2021).
- 1180  
1181 68. Y. Renardy, S. Popinet, L. Duchemin, M. Renardy, S. Zaleski, C. Josserand, ... and  
1182 D. Quéré, “Pyramidal and toroidal water drops after impact on a solid surface,” *J.*  
1183 *Fluid Mech.* **484**, 69-83 (2003).
- 1184  
1185 69. A. Mongruel, V. Daru, F. Feuillebois, and S. Tabakova , "Early post-impact time  
1186 dynamics of viscous drops onto a solid dry surface", *Phys. Fluids* **21**, 032101 (2009).
- 1187  
1188 70. A. I. Fedorchenko, and A. B. Wang, “The formation and dynamics of a blob on free  
1189 and wall sheets induced by a drop impact on surfaces,” *Phys. Fluids* **16**, 3911–3920  
1190 (2004).
- 1191



- 1192 71. S. A. Banitabaei and A. Amirfazli, "Droplet impact onto a solid sphere: Effect of  
1193 wettability and impact velocity," *Phys. Fluids* **29**, 062111 (2017).
- 1194 72. Z. Jian, C. Josserand, S. Popinet, P. Ray and S. Zaleski, "Two mechanisms of droplet  
1195 splashing on a solid substrate," *J. Fluid Mech.* **835**, 1065-1086 (2018).
- 1196  
1197 73. Z. Fan, D. Liu, S. Pan, J. Ma, and X. Chen, "Spreading dynamics of the viscous  
1198 droplet impacting on a spherical particle," *Phys. Fluids* **35**, 023311 (2023).
- 1199  
1200 74. K. Duraisamy, G. Iaccarino, and H. Xiao, "Turbulence Modeling in the Age of Data,"  
1201 *Annu. Rev. Fluid Mech.* **51**, 357-377 (2019).
- 1202  
1203 75. M. Ma, J. Lu, and G. Tryggvason, "Using statistical learning to close two-fluid  
1204 multiphase flow equations for a simple bubbly system," *Phys. Fluids.* **27**, 092101  
1205 (2015).
- 1206  
1207 76. M. Pierzyna, D. A. Burzynski, S. E. Bansmer, and R. Semaan, "Data-driven splashing  
1208 threshold model for drop impact on dry smooth surfaces," *Phys. Fluids.* **33**, 123317  
1209 (2021).
- 1210  
1211 77. V. Vilela, F. J. de Souza, "A Numerical Study on Droplet-Particle Collision," *Flow*  
1212 *Turbulence Combust* **105**, 965–987 (2020).
- 1213  
1214 78. F. Rosenblatt, "The Perceptron, a perceiving and recognizing automaton project  
1215 para," Report Vol. **85**, Nos. 460–461, Cornell Aeronautical Laboratory (1957).
- 1216  
1217 79. Y. He, D. Xiu, "Numerical strategy for model correction using physical constraints,"  
1218 *J. Comput. Phys.* **313**, 617–634 (2016).
- 1219  
1220

- 1221 80. P. S. Koutsourelakis, N. Zabaras, and M. Girolami, "Special Issue: Big data and  
1222 predictive computational modeling," *J. Comput. Phys.* **321**, 1252-1254 (2016).
- 1223  
1224 81. P. Gelss, S. Matera, and C. Schuette, "Solving the master equation without kinetic  
1225 Monte Carlo: tensor train approximations for a CO oxidation model," *J. Comput.*  
1226 *Phys.* **314**, 489–502 (2016).
- 1227  
1228 82. Š. Šikalo, H.-D. Wilhelm, I. V. Roisman, S. Jakirlić, and C. Tropea, "Dynamic contact  
1229 angle of spreading droplets: Experiments and simulations," *Phys. Fluids* **17**, 062103  
1230 (2005).
- 1231  
1232 83. K. Yokoi, D. Vadillo, J. Hinch, and I. Hutchings, "Numerical studies of the influence  
1233 of the dynamic contact angle on a droplet impacting on a dry surface," *Phys. Fluids*  
1234 **21**, 072102 (2009).
- 1235  
1236 84. P. Attané, F. Girard, v. Morin, "An energy balance approach of the dynamics of drop  
1237 impact on a solid surface," *Phys. Fluids* **19**, 012101 (2007).
- 1238  
1239 85. D. E. Rumelhart, G. E. Hinton, and R. J. Williams, "Neurocomputing: Foundations of  
1240 Research, Learning Representations by Back-propagating Errors" MIT Press  
1241 (Cambridge, MA, USA, 1988), 696–699.
- 1242  
1243 86. V. Nair, and G. E. Hinton, "Rectified linear units improve restricted Boltzmann  
1244 machines," In: *Proceedings of 27th International Conference on Machine Learning*  
1245 (2010).
- 1246  
1247 87. D. P. Kingma and J. Ba, "Adam: A method for stochastic optimization," presented at  
1248 the Third International Conference on Learning Representations, San Diego, CA,  
1249 USA, 2015; e-print arXiv:1412.6980.

1250  
1251 88. S. Ruder, “An overview of gradient descent optimization algorithms,” [cs.LG], 2017.

1252  
1253 89. F. Chollet, “Keras,” (2015). <https://keras.io>.

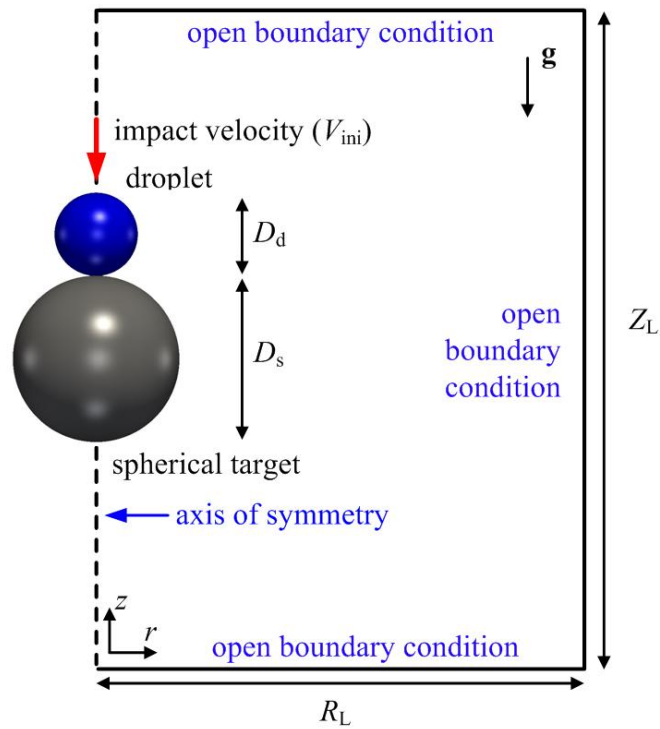
1254  
1255 90. Abadi, M. *et al.*, “TensorFlow: Large-scale machine learning on heterogeneous  
1256 systems,” (2015). Software available from <https://www.tensorflow.org/>

1257  
1258 91. M. A. Nielsen, “Neural Network and Deep Learning,” Determination Press (2015).

1259  
1260  
1261  
1262  
1263  
1264  
1265  
1266  
1267  
1268  
1269  
1270  
1271  
1272  
1273  
1274  
1275  
1276

1277  
1278  
1279  
1280  
1281  
1282  
1283  
1284  
1285  
1286  
1287  
1288

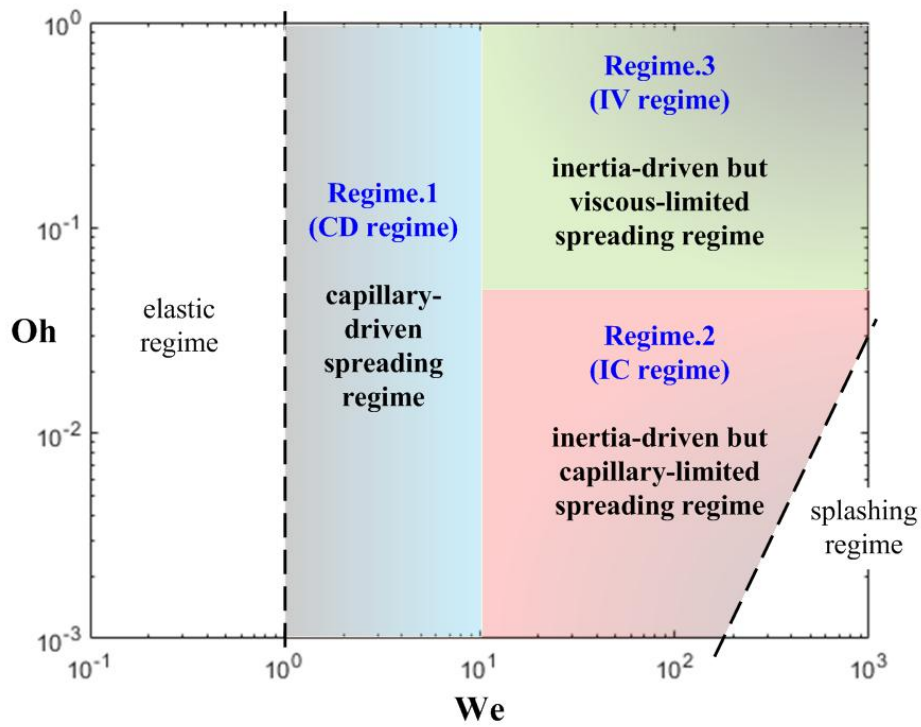
## FIGURES



1289  
1290  
1291  
1292  
1293  
1294  
1295  
1296  
1297  
1298  
1299  
1300  
1301

**Fig. 1.** Simulation geometry and boundary conditions for the droplet impact system.

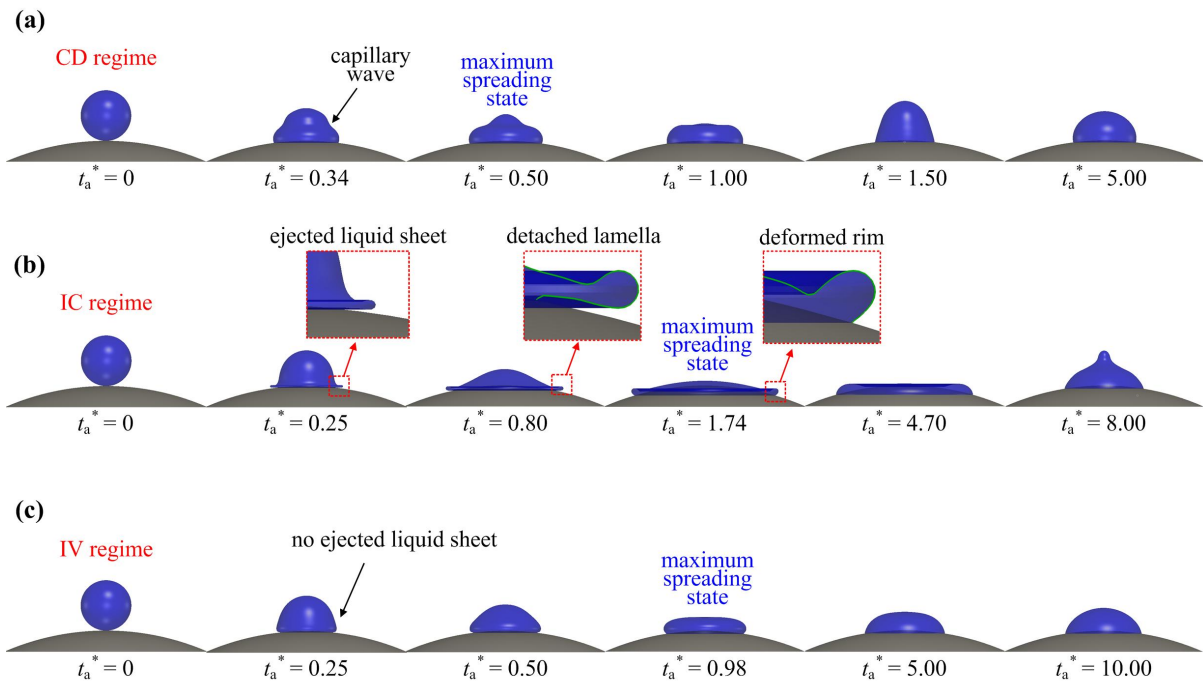
1302  
1303  
1304  
1305  
1306  
1307  
1308  
1309  
1310  
1311  
1312



1313  
1314  
1315  
1316  
1317  
1318

**Fig. 2.** Schematic regime-map for droplet spreading dynamics. Three different spreading regimes, i.e., the capillary-driven (CD), the inertia-driven but capillary-limited (IC), and the inertia-driven but viscous-limited (IV) regimes are marked by the blue, red and green areas, respectively.

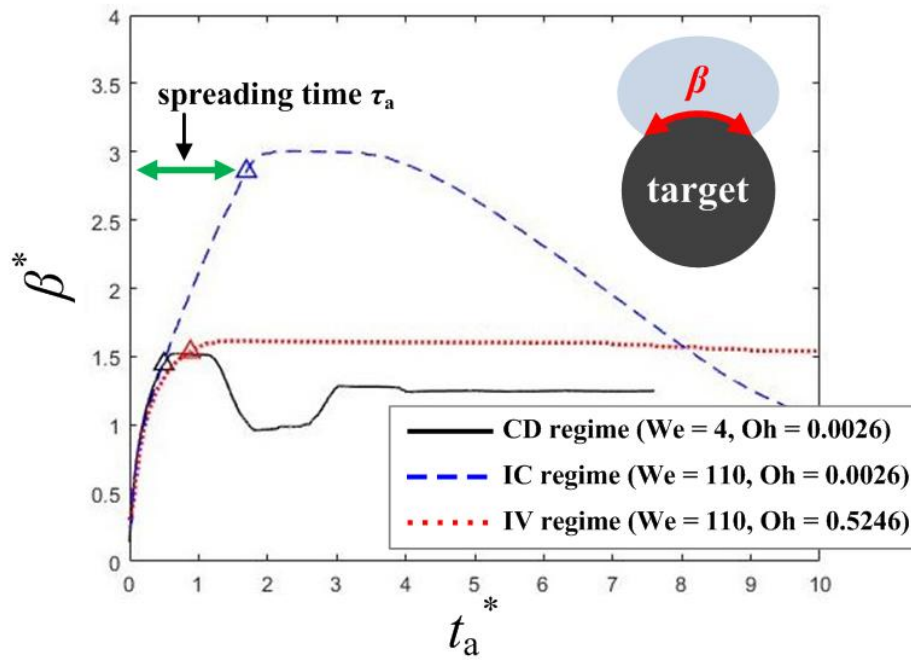
1319  
 1320  
 1321  
 1322  
 1323  
 1324  
 1325  
 1326  
 1327  
 1328  
 1329  
 1330  
 1331



1332  
 1333  
 1334  
 1335  
 1336  
 1337  
 1338  
 1339  
 1340  
 1341  
 1342  
 1343  
 1344  
 1345  
 1346  
 1347  
 1348  
 1349  
 1350  
 1351  
 1352  
 1353

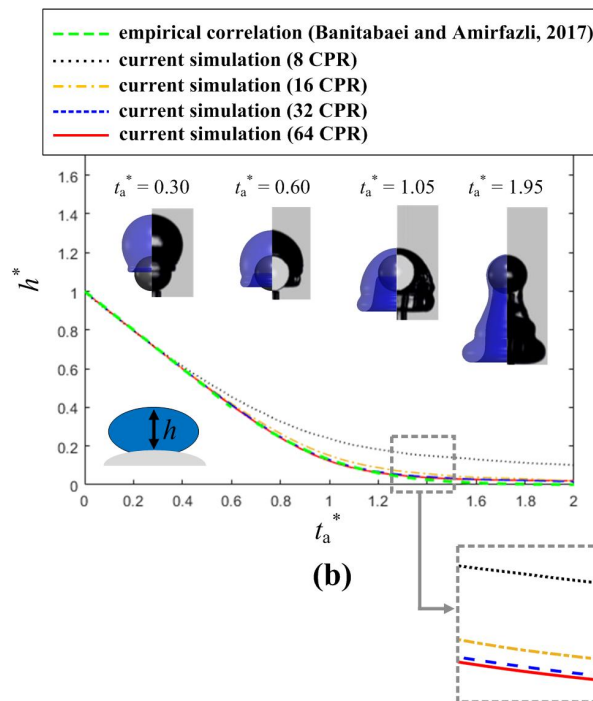
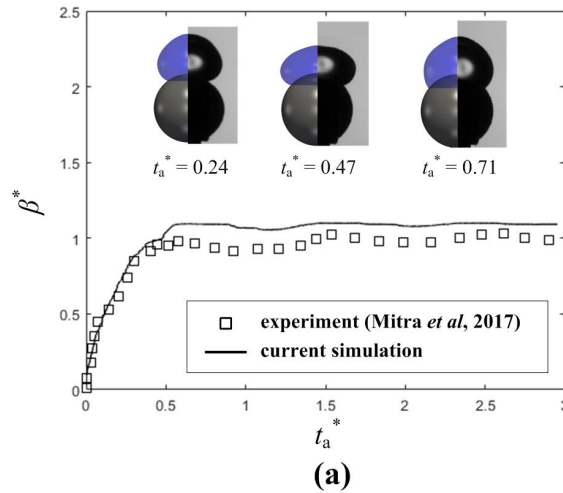
**Fig. 3.** Typical evolution of droplet interfacial morphology for the three different spreading regimes. (a) CD regime ( $We = 4, \theta_{eqi} = 90^\circ$  and  $Oh = 0.0026$ ). (b) IC regime ( $We = 110, \theta_{eqi} = 90^\circ$  and  $Oh = 0.0026$ ). (c) IV regime ( $We = 110, \theta_{eqi} = 90^\circ$  and  $Oh = 0.5246$ ). In these cases,  $\Omega = 1/10$  for generality.

1354  
1355  
1356  
1357  
1358  
1359  
1360  
1361  
1362  
1363



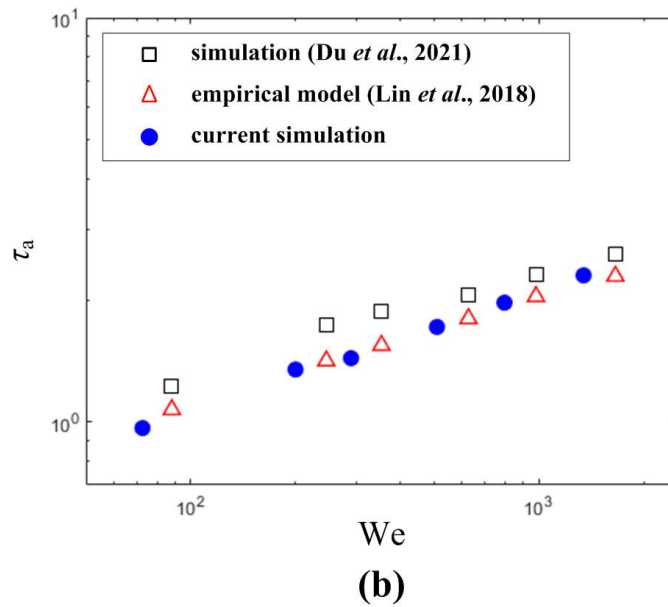
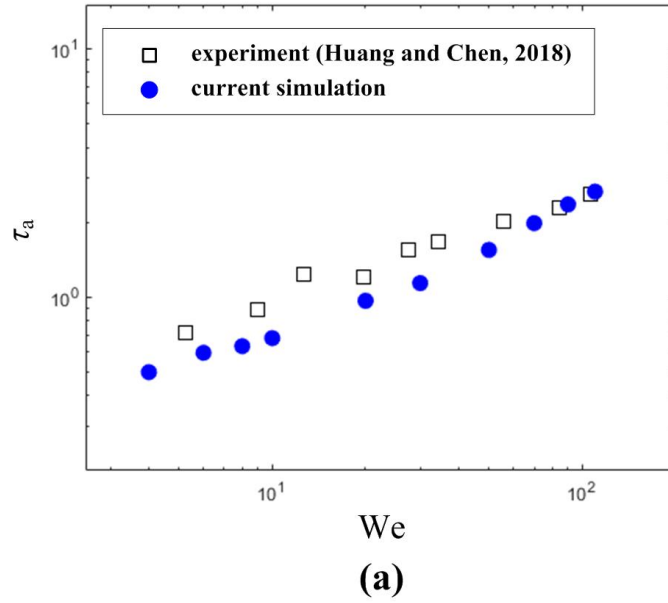
1364  
1365  
1366  
1367  
1368  
1369  
1370  
1371  
1372  
1373  
1374  
1375  
1376  
1377  
1378  
1379  
1380  
1381  
1382

**Fig. 4.** Typical evolution of the non-dimensional spreading extent,  $\beta^*$ , for the three different spreading regimes. All collision conditions for each regime are the same as Fig.3. The inset depicts the schematic for measuring  $\beta^*$ . The spreading times (the time that a droplet attains 95 % of the maximum value of  $\beta^*$ ) are also marked by the triangles.



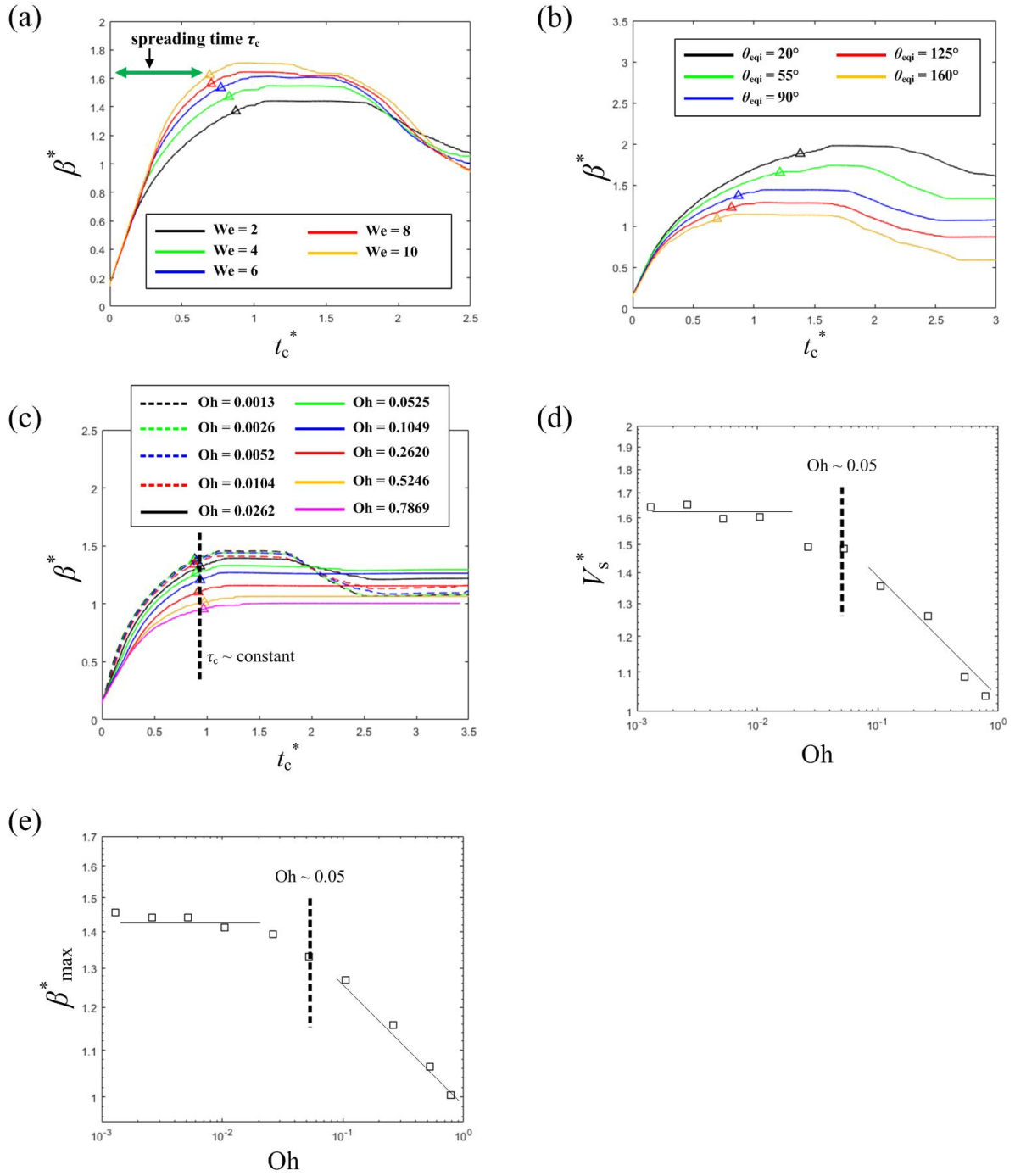
1383  
 1384 **Fig. 5.** Benchmark tests. (a) Evolution of the non-dimensional spreading extent,  $\beta^*$ , for a  
 1385 droplet spreading on a small **spherical target** at low  $We$  ( $We = 0.9$ ,  $\theta_{eqi} = 85^\circ$ ,  $Oh = 0.0026$   
 1386 and  $\Omega = 0.83$ ). The insets compare the interfacial shapes between the experiment [2] and the  
 1387 current simulation for 3 different time instants ( $t_a^* = 0.24, 0.47, \text{ and } 0.71$ ). Reproduced with  
 1388 permission from S. Mitra *et al.*, “Interactions in droplet and particle system of near unity size  
 1389 ratio,” *Chem. Eng. Sci.* **170**, 154–175 (2017). Copyright 2017 Elsevier, Ltd. (b) Evolution of  
 1390 the non-dimensional film thickness,  $h^*$ , for a droplet spreading on a small **spherical target**  
 1391 at high  $We$  ( $We = 155.5$ ,  $\theta_{eqi} = 97^\circ$ ,  $Oh = 0.0026$  and  $\Omega = 1.7$ ) simulated by using 4 different  
 1392 grid resolutions (8, 16, 32 and 64 CPR). The insets compare the interfacial shapes between  
 1393 the experiment [71] and the current simulation for 4 different time instants ( $t_a^* = 0.30, 0.60,$   
 1394  $1.05$  and  $1.95$ ), whereas the other inset in the lower-left corner depicts the schematic for  
 1395 measuring  $h$ . Reproduced with permission from S. A. Banitabaei and A. Amirfazli, “Droplet  
 1396 impact onto a solid sphere: Effect of wettability and impact velocity,” *Phys. Fluids* **29**,  
 1397 062111 (2017). Copyright 2017 AIP Publishing LLC.  
 1398





1399  
 1400  
 1401  
 1402  
 1403  
 1404  
 1405  
 1406  
 1407  
 1408  
 1409

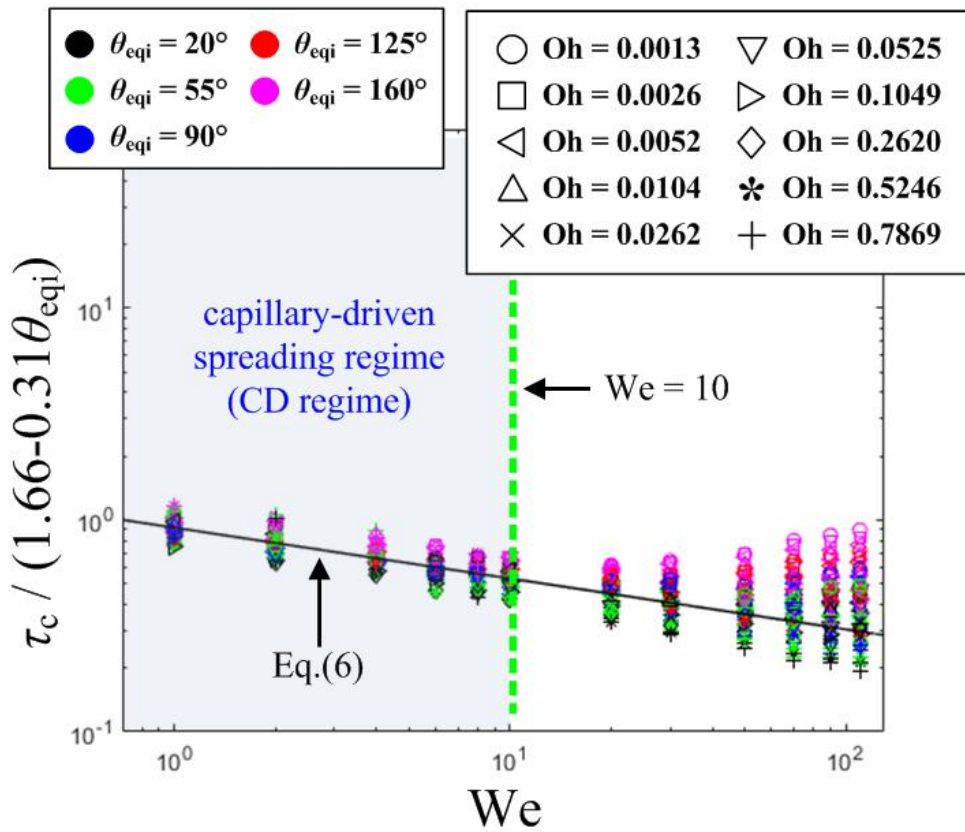
**Fig. 6.** Benchmark tests. (a) Non-dimensional advective spreading time,  $\tau_a$ , at low Oh (Oh = 0.0026). The existing experimental result [18] is marked by black squares. (b)  $\tau_a$  at high Oh (Oh = 0.62). The existing results from the numerical simulation [21] and the empirical correlation [19] are marked by black squares and red triangles, respectively.



1410  
1411  
1412  
1413  
1414  
1415  
1416  
1417  
1418  
1419  
1420  
1421  
1422

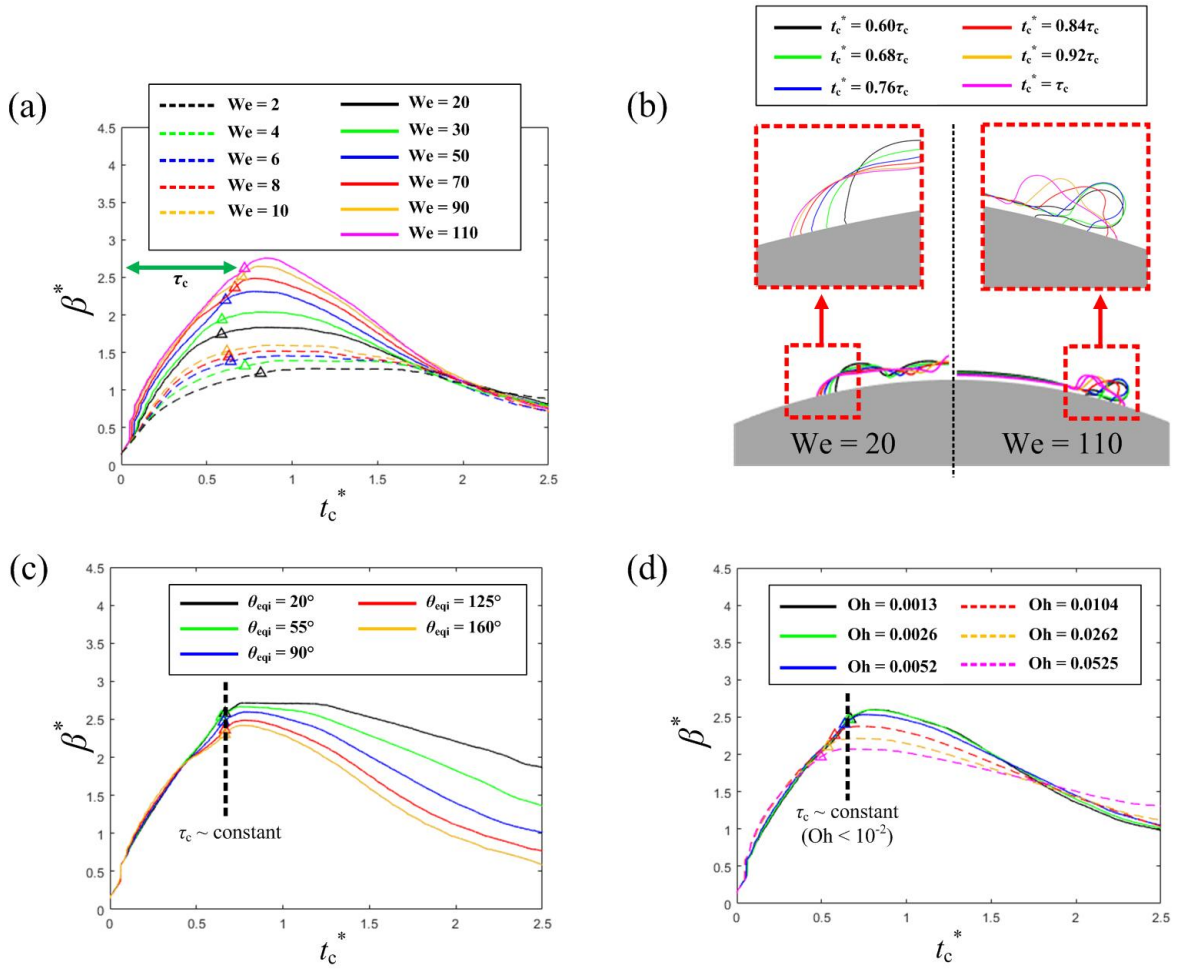
**Fig. 7.** Effect of the impact parameters on  $\tau_c$  for the CD regime. (a) Effect of  $We$  ( $We = 2-10$ ,  $\theta_{eqi} = 90^\circ$  and  $Oh = 0.0026$ ). (b) Effect of  $\theta_{eqi}$  ( $We = 2$ ,  $\theta_{eqi} = 20^\circ-160^\circ$  and  $Oh = 0.0026$ ). (c) Effect of  $Oh$  ( $We = 2$ ,  $\theta_{eqi} = 90^\circ$  and  $Oh = 0.0013-0.7869$ ). (d) Effect of  $Oh$  on the non-dimensional spreading velocity,  $V_s^*$ . (e) Effect of  $Oh$  on the non-dimensional maximum spreading extent,  $\beta_{max}^*$ . For (d) and (e), all collision conditions are the same as Fig.7(c).

1423  
1424  
1425



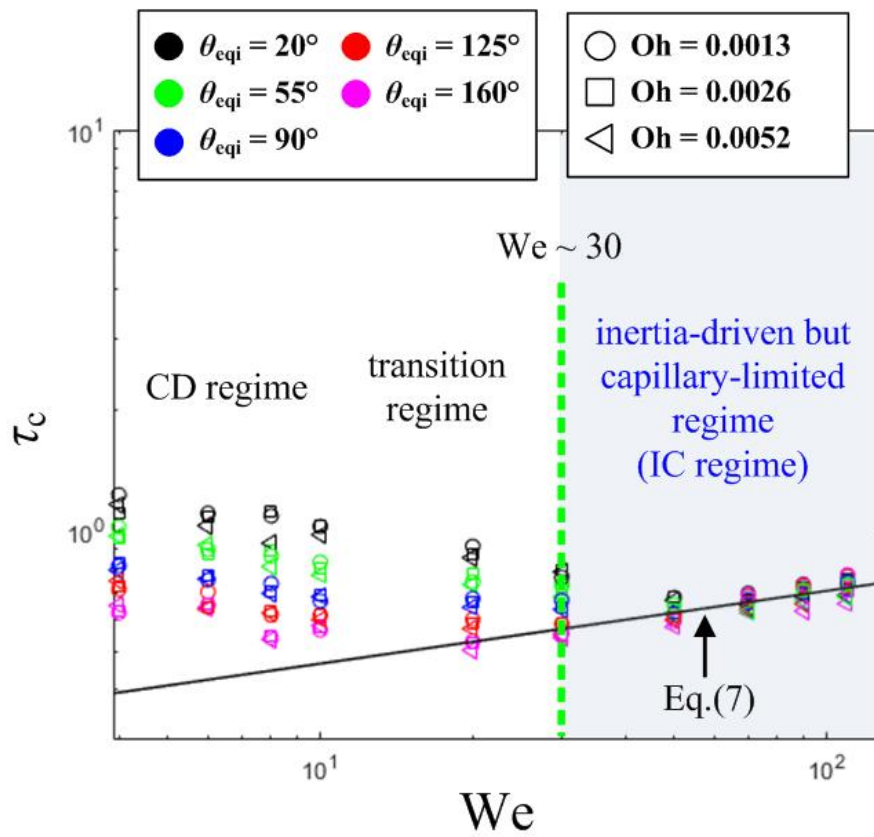
1426  
1427  
1428  
1429  
1430  
1431  
1432  
1433  
1434  
1435  
1436  
1437  
1438  
1439

**Fig. 8.** A total of 600  $\tau_c$  data ( $We = 1-110$ ,  $\theta_{eqi} = 20^\circ-160^\circ$  and  $Oh = 0.0013-0.7869$ ). The proposed prediction model, i.e., Eq.(6) for the CD regime is indicated by the black solid line. The green dashed line depicts the threshold for the CD regime.

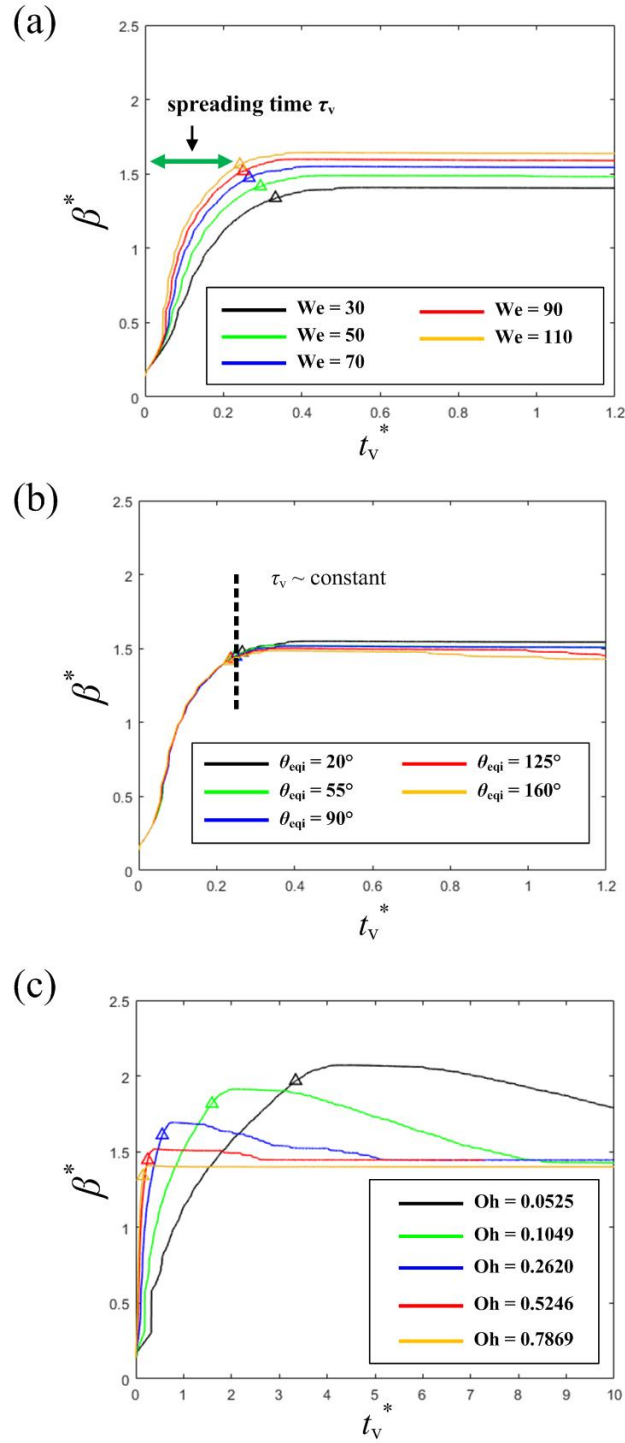


1440  
1441  
1442  
1443  
1444  
1445  
1446  
1447  
1448  
1449  
1450  
1451  
1452  
1453

**Fig. 9.** Effect of the impact parameters on  $\tau_c$  for the IC regime. (a) Effect of We (We = 20–110,  $\theta_{eqi} = 125^\circ$  and Oh = 0.0026). (b) Effect of We on the interfacial evolution of a droplet and its lamella deformation (We = 20 and 110,  $\theta_{eqi} = 20^\circ$  and Oh = 0.0026). (c) Effect of  $\theta_{eqi}$  (We = 90,  $\theta_{eqi} = 20^\circ$ – $160^\circ$  and Oh = 0.0026). (d) Effect of Oh (We = 70,  $\theta_{eqi} = 90^\circ$  and Oh = 0.0013–0.0525).



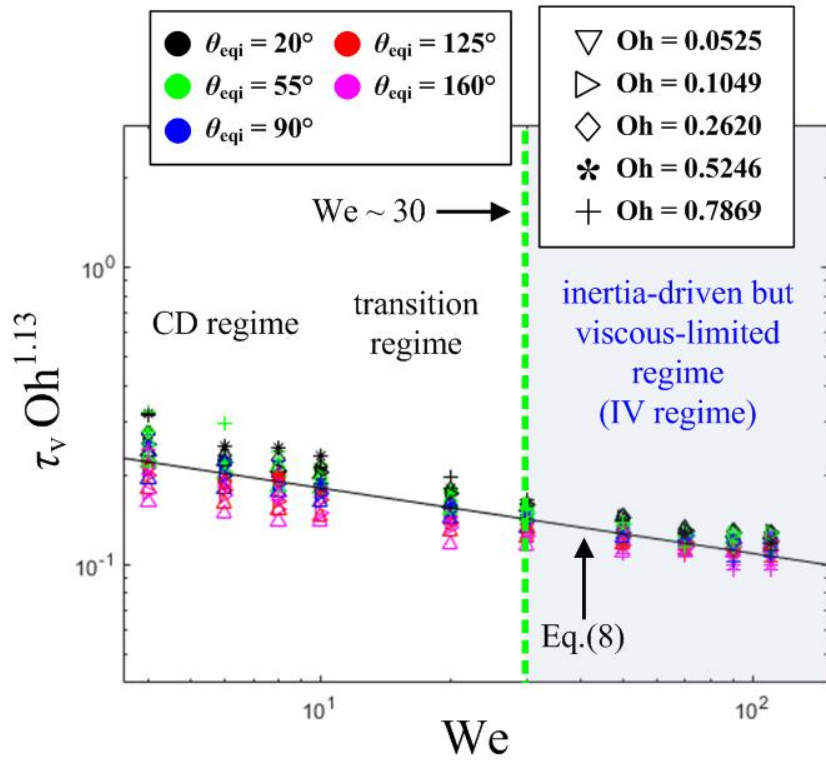
1454 **Fig. 10.** A total of 150  $\tau_c$  data ( $We = 4\text{--}110$ ,  $\theta_{\text{eqi}} = 20^\circ\text{--}160^\circ$  and  $Oh = 0.0013\text{--}0.0052$ ). The  
 1455 proposed prediction model, i.e., Eq.(7), for the IC regime is indicated by the black solid line.  
 1456 The green dashed line depicts the threshold for the IC regime.  
 1457  
 1458  
 1459  
 1460  
 1461  
 1462  
 1463  
 1464  
 1465  
 1466  
 1467  
 1468  
 1469  
 1470  
 1471  
 1472  
 1473  
 1474  
 1475  
 1476



1477  
1478  
1479  
1480  
1481  
1482  
1483  
1484  
1485  
1486  
1487

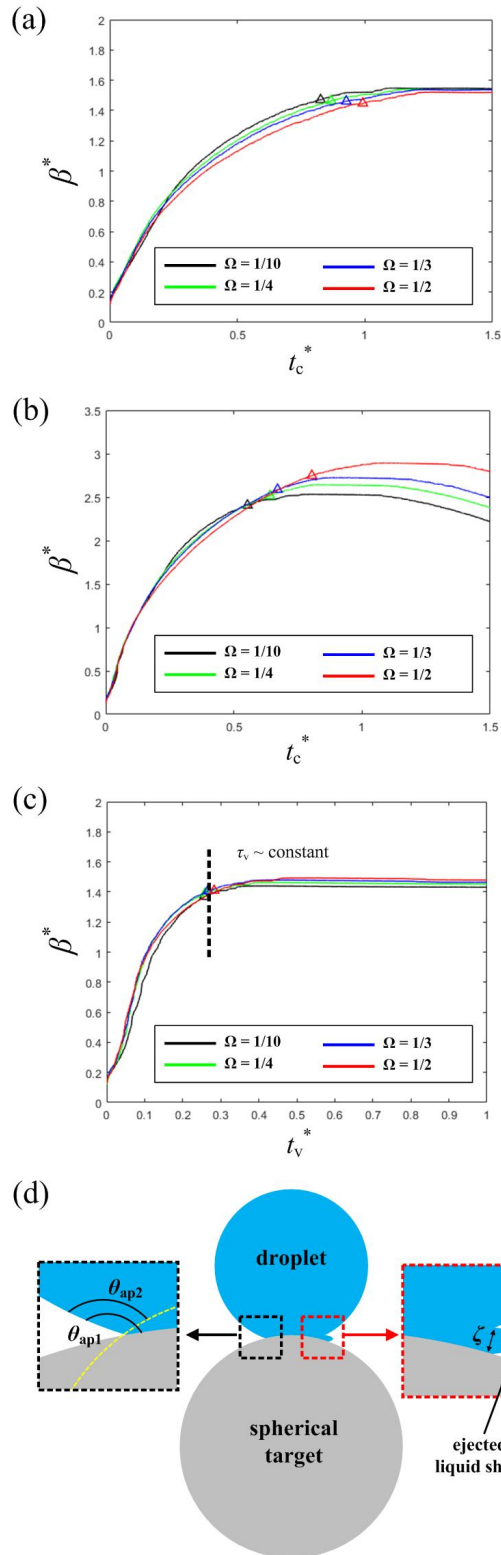
**Fig. 11.** Effect of the impact parameters on  $\tau_v$  for the IV regime. (a) Effect of  $We$  ( $We = 30$ – $110$ ,  $\theta_{eqi} = 20^\circ$  and  $Oh = 0.5246$ ). (b) Effect of  $\theta_{eqi}$  ( $We = 70$ ,  $\theta_{eqi} = 20^\circ$ – $160^\circ$  and  $Oh = 0.5246$ ). (c) Effect of  $Oh$  ( $We = 70$ ,  $\theta_{eqi} = 90^\circ$  and  $Oh = 0.0525$ – $0.7869$ ).

1488  
 1489  
 1490



1491  
 1492  
 1493  
 1494  
 1495  
 1496  
 1497  
 1498  
 1499  
 1500  
 1501  
 1502  
 1503  
 1504  
 1505  
 1506  
 1507  
 1508  
 1509  
 1510  
 1511  
 1512

**Fig. 12.** A total of 250  $\tau_c$  data ( $We = 4-110$ ,  $\theta_{eqi} = 20^\circ-160^\circ$  and  $Oh = 0.0525-0.7869$ ). The proposed prediction model, i.e., Eq.(8), for the IV regime is indicated by the black solid line. The green dashed line depicts the threshold for the IV regime.

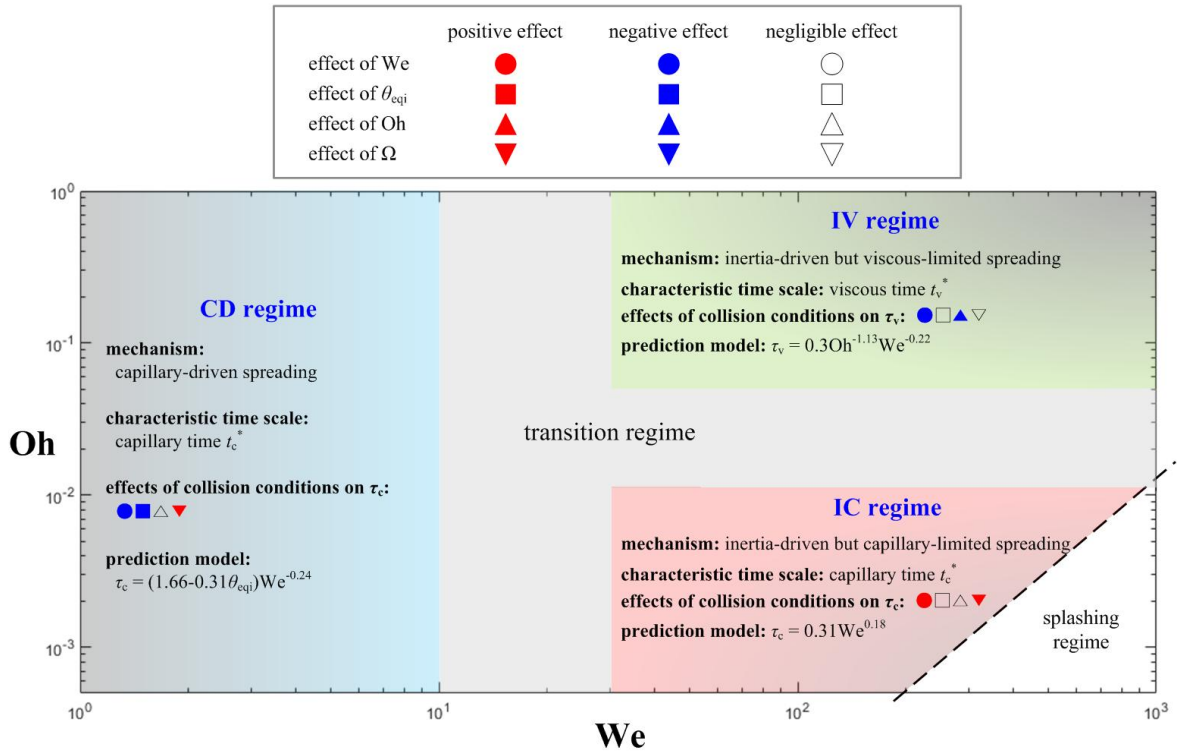


1513  
 1514  
 1515  
 1516  
 1517  
 1518  
 1519  
 1520

**Fig. 13.** (a) Effect of  $\Omega$  on  $\tau_c$  for the CD regime ( $We = 4$ ,  $\theta_{eqi} = 90^\circ$ , and  $Oh = 0.0026$ ). (b) Effect of  $\Omega$  on  $\tau_c$  for the IC regime ( $We = 50$ ,  $\theta_{eqi} = 90^\circ$  and  $Oh = 0.0026$ ). (c) Effect of  $\Omega$  on  $\tau_v$  for the IV regime ( $We = 50$ ,  $\theta_{eqi} = 90^\circ$  and  $Oh = 0.5246$ ). (d) Schematics of the initial apparent contact angles (on the left side) and the lamella characteristics (on the right side).



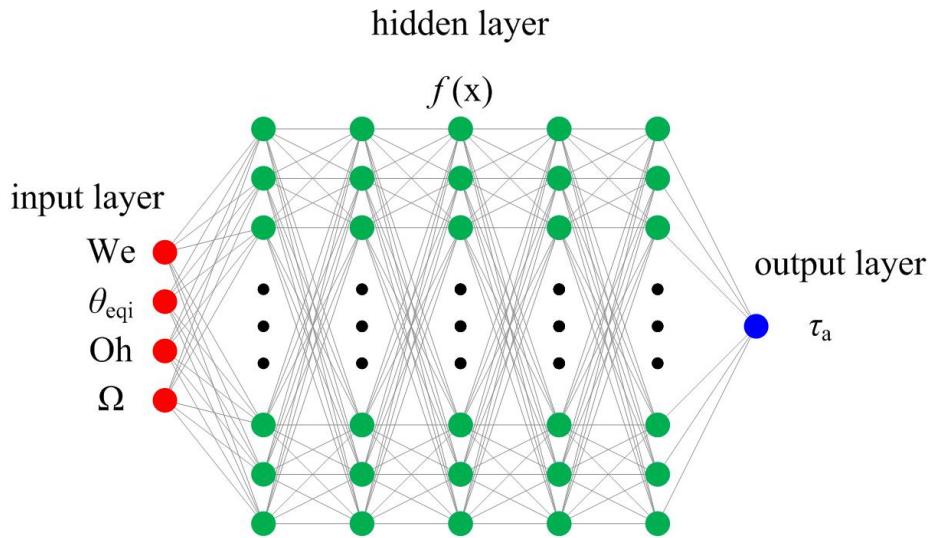
1521  
 1522  
 1523  
 1524  
 1525  
 1526



1527  
 1528  
 1529  
 1530  
 1531  
 1532  
 1533  
 1534  
 1535  
 1536  
 1537  
 1538  
 1539  
 1540  
 1541  
 1542  
 1543  
 1544  
 1545  
 1546  
 1547  
 1548  
 1549  
 1550

**Fig. 14.** Refined regime-map of the droplet spreading mechanism. Three different spreading regimes, i.e., CD, IC, and IV regimes with the transition area are depicted. The physical mechanism driving the spreading process, the characteristic time scale, the effects from 4 impact parameters (We,  $\theta_{eqi}$ , Oh, and  $\Omega$ ) and the prediction models are also presented for each regime.

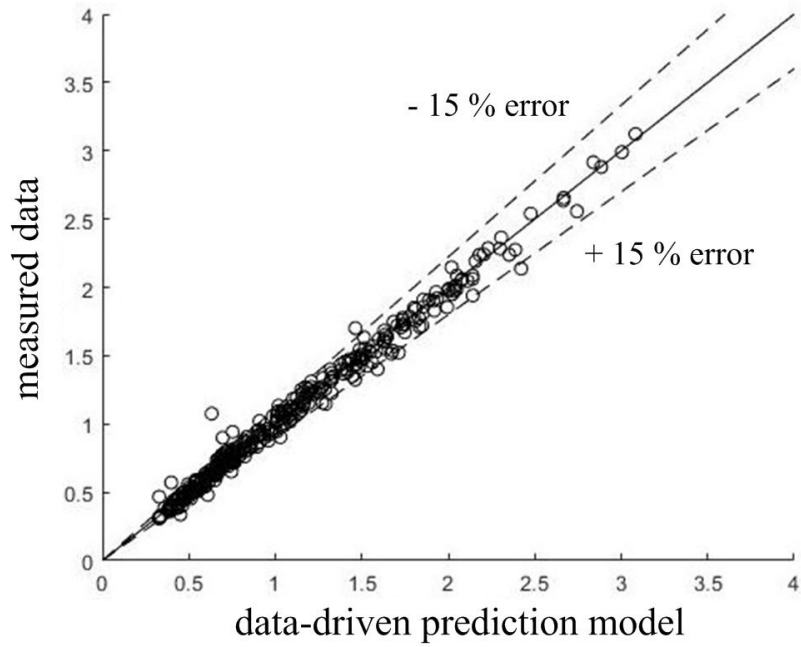
1551  
1552  
1553  
1554  
1555  
1556  
1557  
1558



1559  
1560  
1561  
1562  
1563  
1564  
1565  
1566  
1567  
1568  
1569  
1570  
1571  
1572  
1573  
1574  
1575  
1576  
1577  
1578  
1579  
1580  
1581  
1582  
1583  
1584

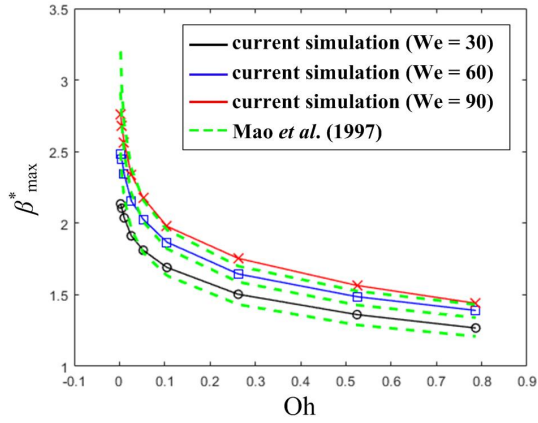
**Fig. 15.** Schematic diagram of the multilayer perceptron (MLP) used in the current study.

1585  
1586  
1587  
1588  
1589  
1590  
1591

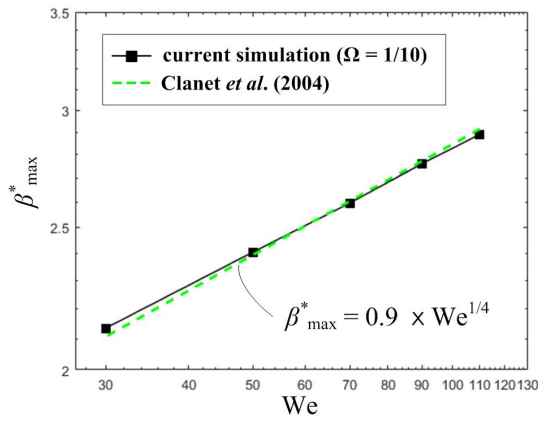


1592  
1593  
1594  
1595  
1596  
1597  
1598  
1599  
1600  
1601  
1602  
1603  
1604  
1605  
1606  
1607  
1608  
1609  
1610  
1611  
1612  
1613  
1614  
1615  
1616

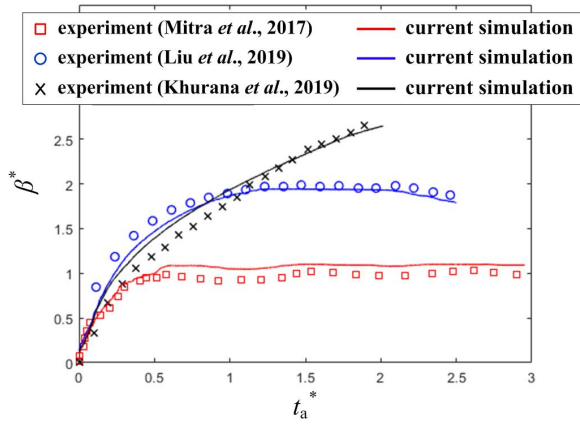
**Fig. 16.** Comparison of the spreading time,  $\tau_a$ , between predicted data by using the data-driven (MLP) model and true (measured) data obtained by our simulations. The deviation range of  $\pm 15\%$  is marked by the two dashed-black lines.



(a)



(b)

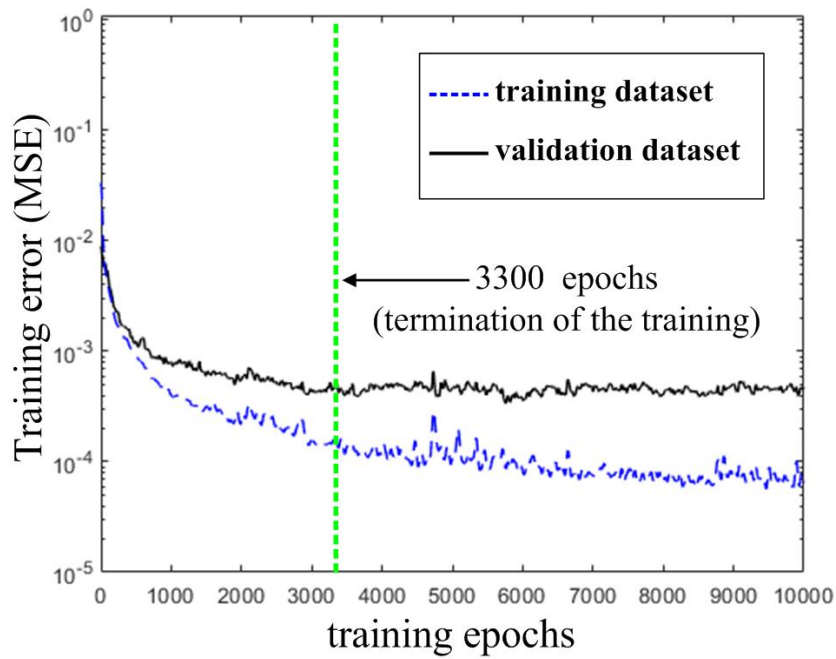


(c)

1617  
1618  
1619  
1620  
1621  
1622  
1623  
1624  
1625  
1626  
1627  
1628

**Fig. 17.** Validation comparisons between our simulation results and existing experimental results. (a) Comparison with Mao *et al.*'s [25] semi-empirical model for droplet impact with a flat surface ( $30 \leq We \leq 90$ ,  $0.0013 \leq Oh \leq 0.7869$ ). (b) Comparison with Clanet *et al.*'s [16] empirical scaling law for droplet impact with a flat surface ( $30 \leq We \leq 110$ ,  $Oh = 0.0026$ ). (c) comparisons with the experimental data of Mitra *et al.* (red squares;  $We = 0.9$ ,  $\Omega = 0.83$ ,  $\theta_{eqi} = 85^\circ$ ,  $Oh = 0.0024$ ) [2], Liu *et al.* (blue circles;  $We = 19.2$ ,  $\Omega = 0.15$ ,  $\theta_{eqi} = 93^\circ$ ,  $Oh = 0.0022$ ) [38], and Khurana *et al.* (black crosses;  $We = 35.3$ ,  $\Omega = 0.60$ ,  $\theta_{eqi} = 85^\circ$ ,  $Oh = 0.0022$ ) [39] for droplet impact with a spherical target. Reproduced with permission from I. Yoon and S. Shin [40], "Maximal spreading of droplet during collision on particle: effects of liquid viscosity and surface curvature," *Phys. Fluids* 33, 083310 (2021). Copyright 2021 AIP Publishing LLC.

1629  
1630  
1631  
1632  
1633  
1634  
1635  
1636  
1637  
1638  
1639  
1640  
1641  
1642  
1643



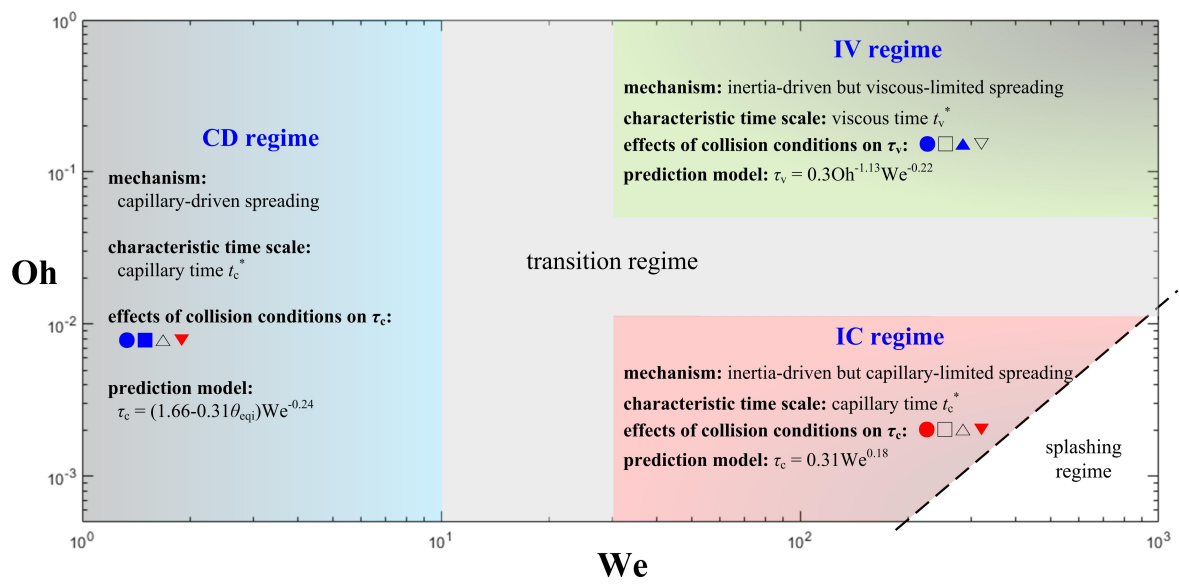
1644  
1645  
1646  
1647  
1648  
1649  
1650  
1651  
1652  
1653  
1654  
1655  
1656  
1657  
1658  
1659  
1660

**Fig. 18.** Training errors (MSE) vs. training epochs for training and validation datasets. The training is terminated at 3300 training epochs where the MSE for the validation dataset (see black solid line) is sufficiently converged. The error for the validation dataset is  $4.62 \times 10^4$ .

1661  
 1662  
 1663  
 1664  
 1665  
 1666  
 1667  
 1668  
 1669  
 1670  
 1671  
 1672

## GRAPHICAL ABSTRACT

	positive effect	negative effect	negligible effect
effect of We	●	●	○
effect of $\theta_{eqi}$	■	■	□
effect of Oh	▲	▲	△
effect of $\Omega$	▼	▼	▽



1673  
 1674  
 1675